Study of Nuclear Dependence of Production and Decay of Φ meson in 12-GeV p+A Interaction

AUTHOR(S):

Yokkaichi, Satoshi

CITATION:

Yokkaichi, Satoshi. Study of Nuclear Dependence of Production and Decay of Φ meson in 12-GeV p+A Interaction. Memoirs of the Faculty of Science, Kyoto University. Series of physics, astrophysics, geophysics and chemistry 2000, 41(1): 181-230

ISSUE DATE:

2000-03

URL:

http://hdl.handle.net/2433/257652

Memoirs of the Faculty of Science, Kyoto University, Series of Physics, Astrophysics, Geophysics and Chemistry, Vol. XXXXI, No. 1, Article 3, 2000

Study of Nuclear Dependence of Production and Decay of ϕ meson in 12-GeV p + A Interaction

By

Satoshi Yokkaichi

Department of Physics, Faculty of Science, Kyoto University
Kyoto 606-8502, Japan

(Received December 20, 1999)

Abstract

We have observed ϕ mesons in the $\phi \to K^+K^-$ decay mode in 12-GeV $p + A$ interaction with the newly constructed spectrometer at the primary beam line in the KEK Proton Synchrotron. The kinematical region of the observed ϕ mesons covers 1 to 3 in $\beta\gamma_{lab}$ where modification of ϕ meson in nuclear matter is expected to be visible. The shape of the invariant mass spectra of the observed ϕ mesons are consistent with that observed in free space within the experimental errors. The mass number dependence of the production cross section follows A^α (α=0.98±0.10) between carbon and lead nuclei. No significant p_T dependence has been observed on the α parameter.

Contents

Chapter 1

Introduction

The mass and the decay width of hadrons have been studied extensively through the history of particle physics. All these measurements have been done for hadrons in free space. If the vacuum structure was changed from that in free space, those properties should also change. In QCD hadrons are described as confined valence quarks which obtained the effective mass due to the spontaneous breaking of the chiral symmetry. The quark condensate $\langle\bar{q}q\rangle$ is the order parameter of the chiral symmetry indicating how large the symmetry is broken. The quark condensate $\langle\bar{q}q\rangle$ is subject to change in hot (T$\neq$ 0) or dense ($\rho \neq 0$) matter providing a vacuum structure different from that in free space. There are many theoretical studies and predictions about the nature of hadrons in such matter [1, 2]. Although $\langle\bar{q}q\rangle$ is not an observable, the mass of vector mesons can provide a good estimate of $\langle\bar{q}q\rangle$. An experimental observation of the in-medium modification of vector mesons is thus desirable to explore the nature of quark matter.

In hot matter, $\langle\bar{q}q\rangle$ is expected to decrease rapidly to zero around the critical temperature T_c where the QCD phase transition will occur and the chiral symmetry

will be restored. The observed excess in lepton pairs by the CERN heavy-ion experiments may already hint a precursor of the symmetry restoration [3]. Above T_c, quark-gluon plasma (QGP) could be formed and quarks could be no longer *heavy* valence quarks but *light* current quarks.

On the other hand, in dense matter, linear decrease of $\langle\bar{q}q\rangle$ is expected theoretically [4]. Several experimental efforts, including this work, have been started to investigate effects of the partially restored chiral symmetry at normal nuclear-matter density [5, 6, 7, 8].

There are three distinct experimental methods to measure the meson mass directly in nuclear media. The first is to measure the invariant mass of decay products. Through this measurement one determines the dispersion relation of the meson in nuclei, namely the changes of the resonance position and the decay width as functions of the momentum of the meson. The second is to compare branching ratios among different decay channels. In-medium modification in any of the mother particle and the daughter particles can cause a change of the decay rate in media since the decay Q-value possibly becomes different due to the mass shift. The third is to search for a nuclear bound state of such mesons. If a meson reduces its mass in nuclei, the meson could be bound. There is an experiment in GSI in preparation to search such a bound state [9]. Using a similar method, Yamazaki *et al.* observed a mass shift of pion in deeply bound pionic states [10]. Although the relation to the

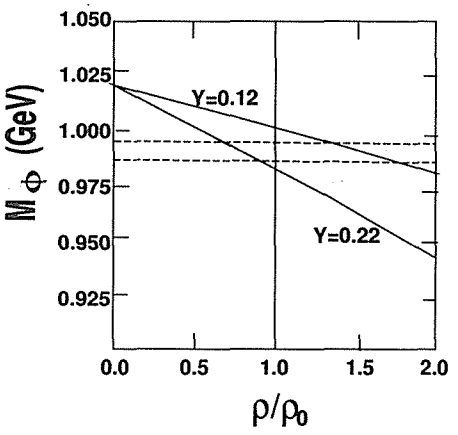

Figure 1.1: Expected mass shift of ϕ meson as a function of nuclear density, where ρ_0 is normal nuclear density. The parameter Y denotes the $2\langle\bar{s}s\rangle_N/(\langle\bar{u}u\rangle_N + \langle\bar{d}d\rangle_N)$ (the strangeness content in the nucleon) and the two lines represent the Y range expected from experimental observations [1].

chiral symmetry is still an open question, studies of deeply bound mesonic states are very interesting possibility on this subject.

We have started an experiment, KEK–PS E325 [8], focusing on the measurements of ϕ meson, both in $\phi \to K^+K^-$ and $\phi \to e^+e^-$ decay modes, for the sake of the unique experimental sensitivities as explained below.

Based on the QCD sum rule, Hatsuda and Lee [1] predicted that the ϕ-meson mass decreases as shown in Figure 1.1. According to this model, the mass decrease of ϕ meson is in the range of 20 to 40 MeV/c^2 at normal nuclear density ρ_0. Although the model predicts larger mass shift for ρ and ω mesons, there are two advantageous aspects in the ϕ-meson decay, namely the signatures to appear in the width and the decay modes.

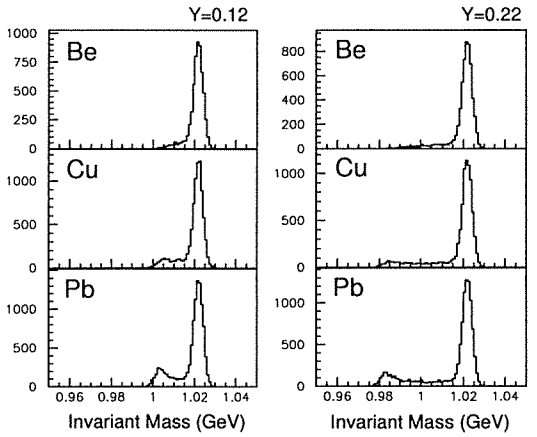

Figure 1.2: Expected invariant mass spectra of ϕ meson for beryllium, copper and lead targets. Definition of Y is as same as Figure 1.1. The left and right columns correspond to the two lines in Figure 1.1.

Figure 1.2 shows the expected invariant mass spectra[†] of the ϕ for beryllium, copper and lead nuclei. In copper case, about 10% of ϕ mesons are expected to decay inside the nucleus. And in the invariant mass spectra, they make the second peak on left side of the main peak which consists of the ϕ mesons decayed outside the nucleus. It should be noted that in the K^+K^- channel, the invariant mass

[†]The Woods–Saxon type nuclear density distribution is employed in the Monte Carlo calculation which treats the ϕ with $\beta\gamma_{lab} \sim 1$. The dispersion of mass in media which is experimentally measurable is neglected in the calculation.

spectra could be deformed due to rescatterings of kaons in nuclei. Measurements in the e^+e^- channel are thus more attractive.

Because decay Q-value is as small as 32MeV in the K^+K^- channel, the decay branching ratios are sensitive to not only ϕ-meson mass shift but also kaon mass shift. Even if the kaon mass is changed and the ϕ-meson mass is unchanged, the effect results in a change of the branching ratios. If the kaon mass is not changed and the ϕ-meson mass decreased more than 32 MeV/c^2, the decay to $K^+K^-$is forbidden in nuclei.

Recently, Klingl *et al.* [11] calculated the in-medium modification of ϕ meson being at rest in nuclear medium using a method to account for the interactions of daughter kaons with the nucleons in nuclear matter. They obtained the mass shift of ϕ meson being consistent with the results of Hatsuda and Lee, with significant broadening of the width as large as 45 MeV/c^2, 10 times larger than in free space. Their calculations was done for the ϕ at rest, and the dispersion, i.e. the width change as a function of the momentum of ϕ meson is yet to be worked out. This calculation, however, implies a significant increase of the decay rate in nuclei for the ϕ mesons in flight and a modification of the invariant-mass shape in the $\phi \to K^+K^-$ channel.

Experimentally a detection of ϕ mesons at rest is nearly impossible since the daughter kaons have too small momentum and decay immediately. Nevertheless, in measurements of the ϕ-meson decays, it is desirable that the momentum of ϕ meson is as low as possible. With the slower ϕ mesons, the larger decay probability inside a nucleus and the larger nuclear matter effect are expected.

It should be noted that the production of ϕ meson with a nuclear target is not well studied so far. The cross section of particle productions with a nuclear target normally follows the relation, $\sigma(A) = \sigma(1) \times A^\alpha$, where A is the nuclear mass number. In the production of the J/ψ and the Drell–Yan lepton-pairs, α is close to unity in high energy, as measured in the $\mu^+\mu^-$ pairs by Binkley *et al.* in 300-GeV/c $n + A$ interaction [12]. To produce those particles it requires partonic interactions like $g + g \to J/\psi$ or $q + \bar{q} \to \gamma^*$, i.e. the production is supposed to be perturbative and all the nucleons in a nucleus contribute equally to the production. In the production of π, ρ and ω mesons α is almost 2/3, which corresponds to the projective surface area of a nucleus. Those particles, consisting of light $u(\bar{u})$ and $d(\bar{d})$ quarks, are produced in the fragmentation, and the yield is supposed to be governed by the first collision of an incident proton whose mean free path in nuclei is much shorter than the typical nuclear radius. On the production of ϕ meson Binkley *et al.* also

showed α to be 0.66 ± 0.03, close to 2/3. However, identification of the ϕ meson here was not perfect due to the poor mass resolution. Bailey *et al.* measured the mass number dependence of the ϕ production in the K^+K^-channel in 120-GeV/c $p + A$ interaction and obtained $\alpha = 0.86 \pm 0.02$ [13]. Aleev *et al.* measured $\phi \rightarrow K^+K^-$ decays in 70-GeV $n + A$ interaction and obtained $\alpha = 0.81 \pm 0.06$ [14]. All the ϕ productions mentioned above were measured in the kinematical region of $0 \leq x_F \leq 0.3$ and $0 \leq p_T \leq 1$ GeV/c. No measurement of the target mass dependence of the ϕ meson production had been performed in the region of $x_F \leq 0$, close to the target rapidity.

The simultaneous measurements of $\phi \rightarrow K^+K^-$ and $\phi \rightarrow e^+e^-$ channels being planned in the present experiment can cancel the effect of unknown production mechanism by taking the ratio of the A-dependence between the both channels, and the media effect on the produced ϕ mesons can be extracted. It is, however, very important and interesting to study the nuclear dependence of the production itself, to understand how the nature of the ϕ reveals in the nuclear interaction.

The experiment E325 has been designed to explore the physics discussed above. The spectrometer newly built for the experiment is located at the primary beam line of KEK 12-GeV Proton Synchrotron. The special emphases are put on the detection of slowly moving ϕ mesons ($\beta\gamma_{lab} \leq 2$) which have a larger probability to decay inside a nucleus, and the simultaneous measurements of $\phi \rightarrow K^+K^-$ decays and $\phi \rightarrow e^+e^-$ decays in the same apparatus. It should be noted that high quality primary beam on thin targets is needed to suppress the background from γ-conversion in the e^+e^- channel.

We started the construction of the spectrometer on June 1996. The engineering run was performed on November 1996, and the first physics run was executed in June 1997, focusing on the $\phi \rightarrow K^+K^-$ decay channel. The results from the run in 1997 are reported in this manuscript.

In Chapter 2, the experimental procedure is described. The analyses procedures are presented in Chapter 3. The invariant mass spectra of ϕ meson and the mass number dependence of the production cross section are presented and discussed in Chapter 4. The conclusion is in Chapter 5.

Chapter 2

Experimental Procedure

The experiment was performed using 12-GeV primary proton beam at the EP1–B beam line in High Energy Accelerator Research Organization (KEK).

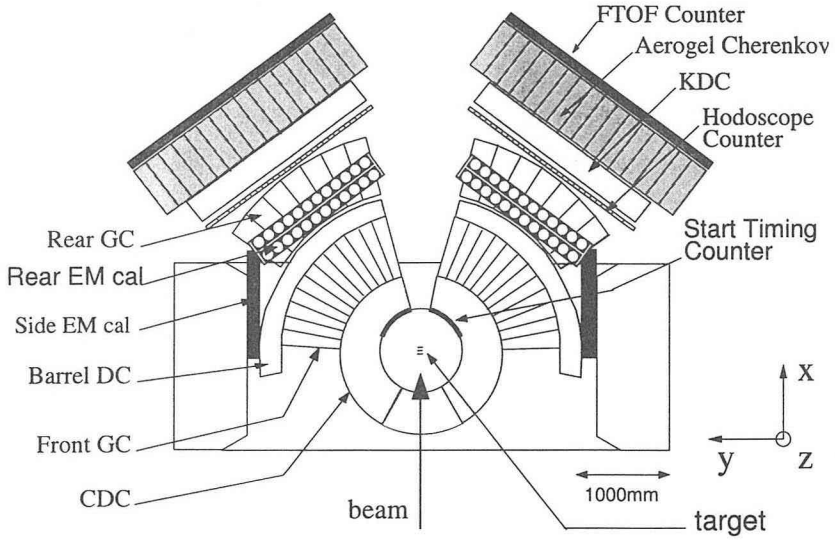

Figure 2.1: Schematic view of the E325 spectrometer, the top view.

Figure 2.1 and 2.2 show a schematic layout of the experiment. Beam protons were delivered to three targets (carbon, lead, and polyethylene) placed in-line at the center of the spectrometer magnet.

The spectrometer has two arms for the kaon and electron detection, sharing the magnet and the tracking devices as common. The kaon arms cover from $\pm 12°$ to $\pm 54°$ horizontally and $\pm 6°$ vertically, where the horizontal angle was measured from the x-axis, the nominal beam-line[†], and the vertical angle was measured from the xy-plane (horizontal plane). The electron arms have a much larger acceptance covering from $\pm 12°$ to $\pm 90°$ horizontally and $\pm 22°$ vertically.

The trajectories and momenta of K^+K^-pairs and e^+e^-pairs from ϕ-meson decays were determined with the Cylindrical Drift Chamber (CDC) and the Bar-

[†]In this manuscript, we adopt the right handed coordinate system of which the origin is at the center of the spectrometer magnet, the x-axis is the nominal beam direction, and the z-axis is vertical pointing upward.

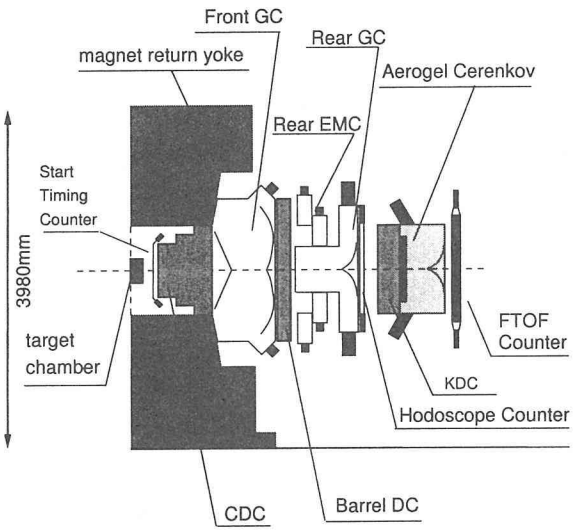

Figure 2.2: Schematic view of the E325 spectrometer. The cross section along the 33 degrees line, the center of the kaon arm, is shown.

rel Drift Chambers (BDC). Kaons were identified with the Time-Of-Flight (TOF) method using the Start Timing Counters (STC) and the Forward TOF Counters (FTOF) in the off-line analysis. The Aerogel Čerenkov counters (AC) and the Hodoscope Counters (HC) were used with FTOF for the on-line trigger to select kaons. Electron identification was performed with the segmented Gas Čerenkov counters (FrontGC / RearGC) and the lead glass EM Calorimeters (SideEMC / RearEMC). Detail descriptions are given in the following subsections.

2.1 Beam line

The beam line EP1–B was specially designed for the primary beam usage requiring small beam halo. The schematic view of the beam-line components is shown in Figure 2.3. In typical operation, a small fraction (1/100) of protons were extracted from PS for the duration of 1.8 sec (spill) with a repetition period of 4 sec. About 2×10^{10} of protons in the ring were delivered to the first vertical collimator $1V$ where the intensity was reduced to one-tenth and the primary image of the beam was defined together with the horizontal collimator 2H. The beam intensity was controlled by changing the aperture of the collimator $1V$. The beam was transported

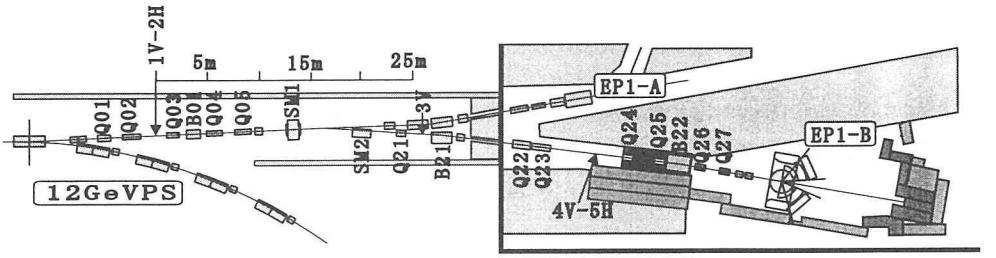

Figure 2.3: EP1–B beam line at KEK–PS North Counter Hall. The collimator positions are indicated with arrows.

to the final focusing point at the center of the spectrometer magnet, where we obtained the beam spot size of 7 mm in FWHM as shown in Fig 2.4. To compensate the beam deflection in the spectrometer magnet, the beam was tilted in the bending magnet B22 from the nominal beam line. At the target point the beam angle is 0.9 degrees from the nominal beam line.

The spectrometer was designed for the operation with 1×10^9 proton/sec on 0.1% interaction target. For the data described in this paper, we used typical intensity of 1.1×10^8 proton/sec with the interaction rate of 1.0×10^6/sec because in this period we triggered only K^+K^-pairs and thin target-thickness to suppress the background electrons was not required. In this period, the spill duration was shortened to 1.2 sec (with a 4-sec repetition period) due to the power supply problem in PS.

Since we did not count beam protons particle by particle because of the high intensity, beam intensity was monitored with 10% accuracy using an ionization chamber [15] located just after the spectrometer.

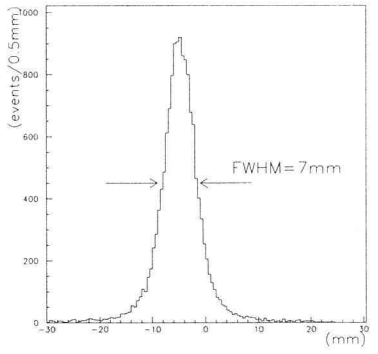

Figure 2.4: Reconstructed beam profile in the y-axis (horizontal).

2.2 Target and target chamber

Lead, carbon and polyethylene were used as target materials. Polyethylene $[(CH_2)_n]$ is used to obtain an effective hydrogen target with CH_2-C subtraction. Their dimensions as well as other properties are listed in Table 2.1. These targets were placed in-line at the center of the spectrometer magnet by 42 mm apart each other. The interaction length is 0.58% in total summed over the three targets.

target	width	height	thickness	interaction length	radiation length
Polyethylene	25mm	20mm	$0.18 g/cm^2 (\sim 2mm)$	0.23%	0.40 %
Carbon	25mm	20mm	$0.20 g/cm^2 (\sim 1mm)$	0.23%	0.46 %
Lead	25mm	20mm	$0.23 g/cm^2 (\sim 0.2mm)$	0.12%	3.65 %

Table 2.1: Target properties.

The schematic view of the target support is shown in Figure 2.5. Lead and carbon foils were held by a pair of 1-mm-thick polyethylene stays which sandwiched each target foil at its lower edge. The longer stay was used as the polyethylene

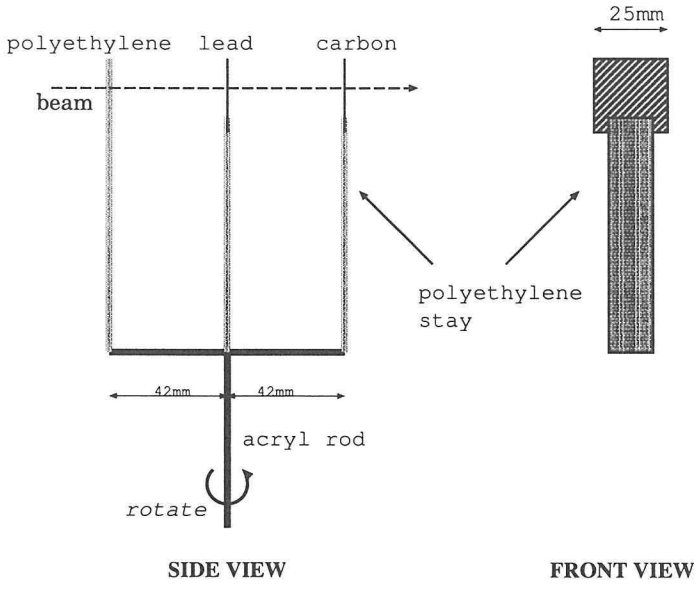

Figure 2.5: Targets and target holder.

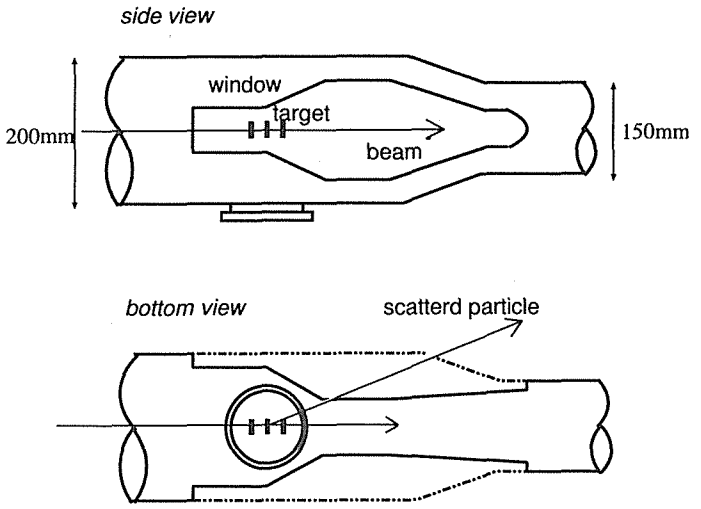

Figure 2.6: Beam pipe and target chamber.

target as it was. The target holder was rotated in every 48 hours to minimize the position dependence of the acceptance for each target.

Primary proton beam was delivered to the experimental area through a vacuum beam pipe. At 4.6 m upstream the center of the spectrometer magnet, the vacuum was terminated with a 200 μm-thick mylar window, and followed by a helium-filled beam pipe. The pipe was directly connected to the target chamber as shown in Fig 2.6. In the target chamber the exit windows to the detector acceptance were covered with 50 μm-thick mylar windows. Downstream the target chamber, a helium-filled beam pipe of 5.5 m long followed. At the end of this pipe, the ionization chamber was mounted for the beam intensity monitoring.

2.3 Spectrometer magnet

The spectrometer magnet was a dipole type recycled from the cyclotron magnet[‡]. The pole gap and the diameter were modified to 907 mm and 1760 mm, respectively. The height of the magnet is 3980 mm, with the width of 5655 mm and the depth of 2120 mm. Other dimensions can be seen in Figure 2.7.

The magnetic field strength was 0.71 T at the center of the spectrometer magnet and $\int Bdl$ was about 0.81 Tm from the center to the radius of 1600 mm where the

[‡]the Frequency Modulation Cyclotron from Institute of Nuclear Study, University of Tokyo.

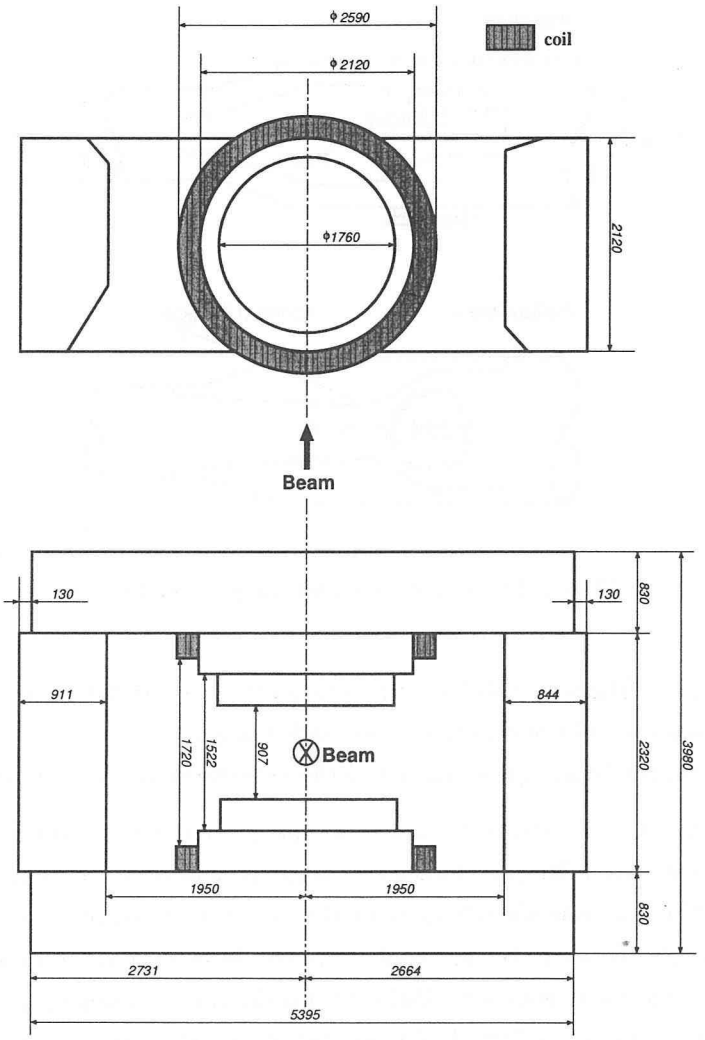

Figure 2.7: Spectrometer magnet.

tracking chambers BDC were located.

We found a good agreement within 0.2% in the difference of $\int Bdl$ between the field measurements and the three-dimensional field calculation using TOSCA which performed the finite element analysis [16]. We thus used the calculated field map for the momentum determination. Systematic error in the momentum $\delta p/p$ due to the field-map uncertainty was evaluated to be within 0.2% as shown in Figure 2.8, which were obtained by generating particle trajectories with the measured map,

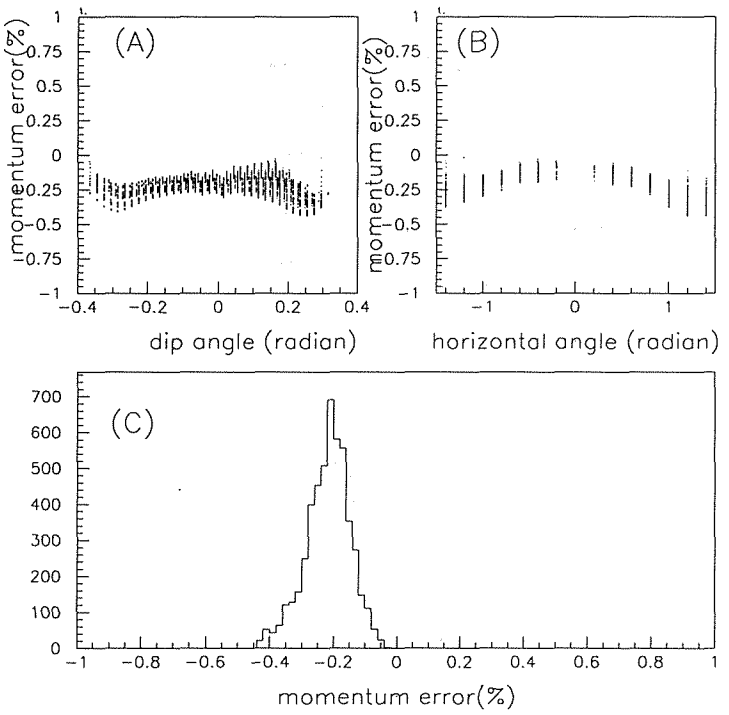

Figure 2.8: Comparison of the measured magnetic field map and the calculated map. Particles were generated with the measured map and reconstructed with the calculated map. The ratios, the reconstructed momentum over the input momentum, are plotted as a function of the vertical angle in (A) and the horizontal angle in (B). The histogram (C) gives the projection of all the ratios.

reconstructing them with the calculated map, and comparing the input momentum with the reconstructed momentum. The generated particles covered all the acceptance and the momentum region from 0.5 GeV/c to 2.0 GeV/c.

2.4 Tracking Chambers

Trajectories of charged particles were determined with the Cylindrical Drift Chamber (CDC) and the two sets of the Barrel Drift Chambers (BDC). The Kaon Drift Chambers (KDC) were prepared to discard kaon decays. The KDCs were not operational for the data taking period of the present analysis.

Figure 2.9 shows the schematic view of CDC whose outer diameter is 1760 mm, the inner diameter is 800 mm and the height is 840 mm.

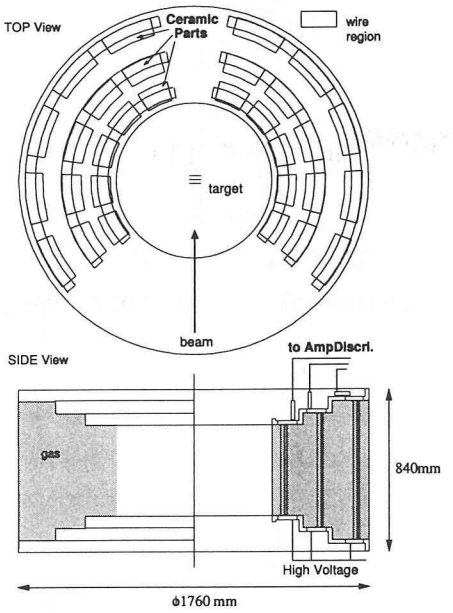

Figure 2.9: Schematic view of CDC.

The CDC was placed on the pole piece of the spectrometer magnet, and the targets were placed at the center. The CDC covers from ±12 degrees to ±132 degrees horizontally and ± 23 degrees vertically with 10 layers of drift cells.

The drift-cell structure is shown in Figure 2.10. The wires were held with a metalic feedthrough on the ceramic boards which have printed circuit patterns on them. The ceramic boards were mounted on the end plates made of aluminum. Each cell in all the layers had the same angular coverage of 1.5 degrees with respect to the target, and the same radial depth of 10 mm.

The layers were grouped into three. The first 3 layers (X, X', U) were in the radial region of 445 to 475 mm, the next 4 layers (V, V', X, X') were in 602.5 to 642.5 mm, and the last 3 layers (U, X, X') were in 800 to 830 mm. In the X and the X' layers the wires were vertical and in the U and the V layers the wires were tilted by about ± 0.1 radian (see Table 2.2 for detail). In the U layer, the top end of the wire were at a lager angle with respect to the beam axis than the bottom end. In the V layer the tilt angle was opposite.

The end plates of CDC looks like a staircase as shown in Figure 2.9, so that all the layers have an almost same coverage in the vertical angle in order to limit the

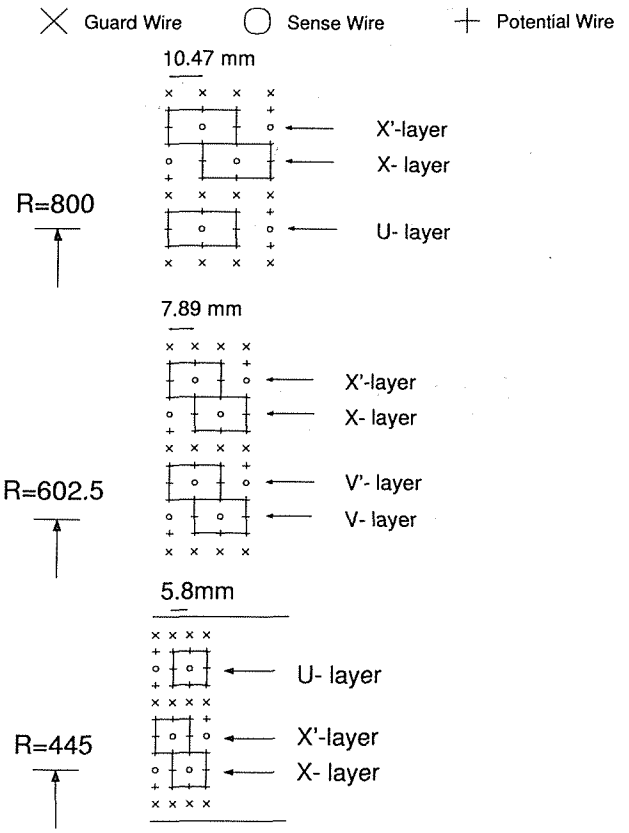

Figure 2.10: Schematic view of the CDC cell structure. Each drift cell is shown with a box with a sense wire at the center (sense wire is shown as a circle).

layer	1	2	3	4	5	6	7	8	9	10
wire direction	X	X'	U	V	V'	X	X'	U	X	X'
radial location of the sense wire position(mm)	445	455	475	602.5	612.5	632.5	642.5	800	820	830
cell width(degree)	1.5	1.5	1.5	1.5	1.5	1.5	1.5	1.5	1.5	1.5
cell width(mm)	11.65	11.91	12.43	15.77	16.04	16.55	16.82	20.94	21.47	21.73
tilt angle(radian)	0	0	0.1127	0.1116	0.1135	0	0	0.1174	0	0
number of sense wire	81	81	77	76/77(*)	77/76(*)	81	81	77	82	82

(*)left-arm and right-arm

Table 2.2: CDC configuration.

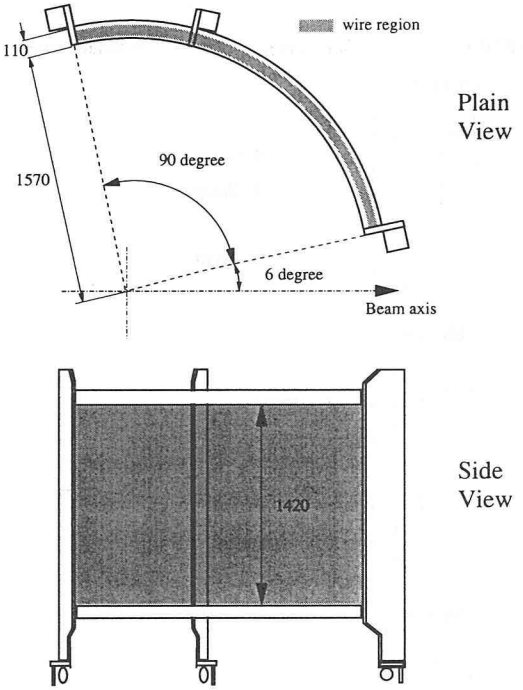

Figure 2.11: Schematic View of BDC. Sizes are given in the unit of mm.

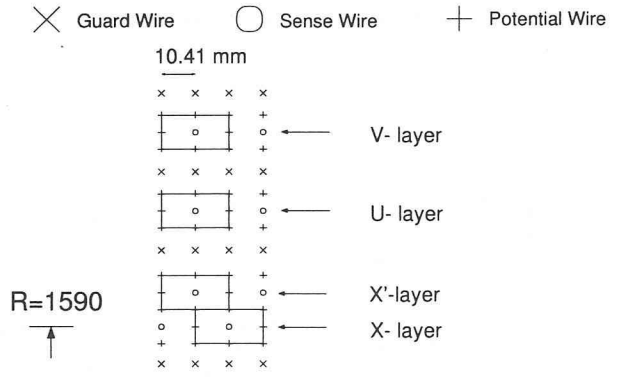

Figure 2.12: Schematic view of the BDC cell structure.

sensitive region of the wires only to the spectrometer acceptance.

The BDCs had 90-degrees arc-shaped endplates at the top and the bottom which are supported by 3 aluminum bars as shown in Figure 2.11. The inner radius was

1570 mm, the outer radius was 1680 mm, and the height was 1420 mm. These chambers were placed outside FGC to cover from ±6 degrees to ±96 degrees horizontally and ±23 degrees vertically. There were 4 layers of drift cells (X, X', U, V) with a cell structure as shown in Figure 2.12. The drift cells in all the four layers had the same angular coverage of 0.75 degrees with respect to the center of the arc, i.e. the target position. They had the same radial depth of 10 mm.

Gas mixture of argon (50%) and ethane (50%) was used for the operation of CDC and BDCs. The anode wires were gold-plated tungsten of 30μmϕ and the potential wires were Be-Cu of 100μmϕ for the both chambers. The detail characteristics of CDC and BDC are summarized in Table 2.2 and 2.3, respectively.

layer	1	2	3	4
wire direction	X	X'	U	V
location of sense wire from the center of the arc(mm)	1590	1600	1620	1640
cell width(degree)	0.75	0.75	0.75	0.75
cell width(mm)	20.81	20.94	21.21	21.47
tilt angle(radian)	0	0	0.1058	0.1071
number of sense wire	116	116	109	109

Table 2.3: BDC configuration.

To obtain a track coordinate from measured drift time, following procedures were carried out. Adjustment of relative time zero (T0) of all the wires was performed by pulsing all the pre-amplifiers via a test input. The average of the obtained peak was subtracted from the measured drift time in each channel. We obtained the reference x-t relation (correlation of the measured time and the drift length) with use of the drift chamber simulation code Garfield [17]. We then iteratively adjusted the common T0 offset and the scaling factors of drift velocity. The scaling factors were chosen to be same for the cells with the same drift distance. For the iteration we used residuals from the tracks obtained by the fitting using the Runge-Kutta method as described in Section 3.3.

We obtained the position resolution of typically less than 400 μm as shown in Figure 2.13. The detail performance of each layer is summarized in Table 2.4 and 2.5.

Through the fitting procedure the efficiency of each layer was also determined. The efficiency of a cirtain layer, $\mathcal{E}(layer)$, is defined as follows:

$$\mathcal{E}(layer) = N_{all}/(N_{off}(layer) + N_{all})$$

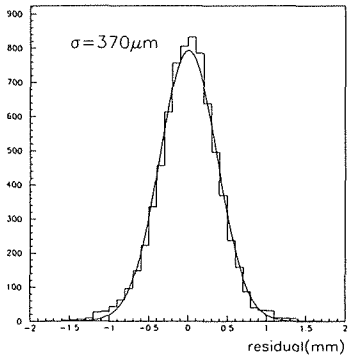

Figure 2.13: CDC resolution.

layer	1	2	3	4	5	6	7	8	9	10
wire direction	X	X'	U	V	V'	X	X'	U	X	X'
typical resolution (μm rms)	440	380	290	350	350	350	350	310	350	410
typical efficiency(%)	96	93	61	95	92	88	91	77	90	80

Table 2.4: CDC performance.

layer	1	2	3	4
wire direction	X	X'	U	V
typical resolution (μm rms)	370	350	110	120
typical efficiency(%)	90	87	70	69

Table 2.5: BDC performance.

Here, N_{all} denotes the number of tracks having hits in all the layers of the chambers (CDC or BDC). And $N_{off}(layer)$ denotes the number of track missing only one hit in the relevant *layer*. It should be noted that this evaluation procedure includes possible difference of the track reconstruction efficiency between the layers. The results are summarized in Table 2.4 and 2.5. Typical efficiency in the X and the X' layers was 90%, and 70 % in the U and the V layers within 3% of variations.

The alignment of BDCs against CDC was determined using straight tracks in the data taken without magnetic field. By adjusting the position in the xy-plane and the rotation angle around the z-axis, we achieved the agreement within 200μm between the hit position in BDCs and the extrapolated position from the straight tracks obtained with the CDC hit positions.

To evaluate the achieved tracking performance, $\Lambda \rightarrow p\pi^-$ decays were studied. In Figure 2.14, the invariant mass spectrum of $p\pi^-$ pairs are plotted. We required the decay points were more than 20 mm apart from the target. The clear peak of Λ shows the mass resolution of 2.2 MeV/c^2.

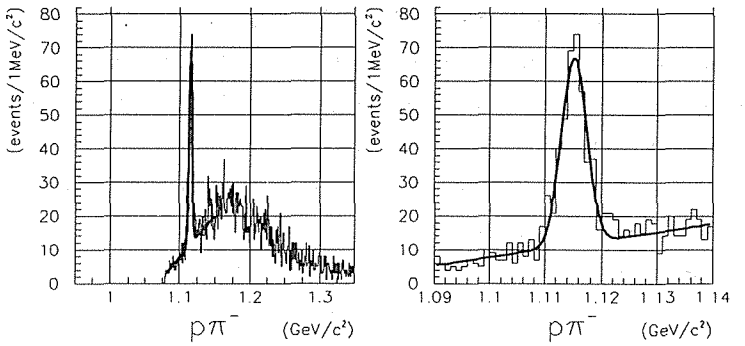

Figure 2.14: The $p\pi^-$ invariant mass spectra. The line is the best fit result of a Gaussian with a linear background. Λ is seen at 1115.11 MeV/c^2 with a resolution of 2.2 MeV/c^2.

By rescaling this mass resolution by taking account of the differences in the Coulomb scattering effects and in the momentum distributions of protons, pions and kaons, we evaluated the mass resolution of the $\phi \rightarrow K^+K^-$ invariant mass to be 1.2 MeV/c^2 , which is slightly worse than the designed values (1.1 MeV/c^2) but good enough for the present analysis.

The peak value of the Gaussian fit is 1115.11 MeV/c^2, which is slightly different from the mass of Λ in the literature [18], 1115.68 MeV/c^2. This implies that there can be some systematic errors remaining in the invariant mass due to the momentum determination, which corresponds to less than 0.3 MeV/c^2 in the $\phi \rightarrow K^+K^-$channel.

2.5 Kaon Identification Counters

2.5.1 Scintillation Counters

Since we did not count the beam particles, the start timing was given by the Start Timing Counters (STC), placed at 380 mm from the center of the spectrometer magnet. The STC consisted of 8 segments of scintillator in each arm.

One segment was 400 mm in height, 40 mm in width and 3 mm in thickness.

The STC covered from ±12 degrees to ±60 degrees horizontally. They were read out with a pair of 2-inch fine-mesh PMT's from the top and the bottom ends. At this location the magnetic field strength was 0.7 T.

The Forward Time-Of-Flight counters (FTOF) were used to give the stop timing. The FTOF consisted of 16 segments of scintillator in each arm. Those covered from ±12 degrees to ±54 degrees horizontally and ±6 degrees vertically. We used two types of scintillator slabs, one was 800 mm in height, 200 mm in width and 30 mm in thickness and the other was 800 mm in height, 170 mm in width and 20 mm in thickness as summarized in Table 2.6. The slabs were arrayed being alternately staggered with an overlap of 2 mm. The time resolution obtained with the STC-FTOF combinations was typically 400 psec[†].

In combination with the FTOF counters, the Hodoscope Counters(HC) were used to determine the sign of charged particles in the 1st-level trigger. And in the 2nd-level trigger, HC were prepared to determine a rough momentum of particles and make the kaon selection possible with the β measurements using FTOF. However, the more simplified version of the 2nd-level trigger logic was used and the HC were not used for the 2nd-level trigger in the experimental period described in this manuscript. Detail of the 2nd level trigger is described in Section 2.8. The HC consisted of 28 segments of scintillator in each arm, and one segment was 2000

counter	STC	HC	AC	FTOF
shape	arc	arc	rectangular	rectangular
distance from the target(mm)	380	2615	3312.5	3951
horizontal coverage(degree)	6∼60	6∼60	6∼54	6∼54
vertical coverage (degree)	±30	±22	±6	±6
number of segments	8	28	16	16
height(mm)	400	2000	(706)	800
width(mm)	40	70	160	200/170
thickness(mm)	3	5	(125)	30/20
horizontal coverage(degree)	6	1.5	∼2.7	∼2.7
PMT (Hamamatsu)	H6154	H1161	H6527	H1949
for the readout	(R5504)	(R329-02)	(R1250)	(R1828-01)

Table 2.6: The structure of the trigger counters, STC, HC, AC and FTOF. The dimensions of AC are the volume of aerogel.

[†]The time resolution was deteriorated in STC due to the pulse height decrease in the magnetic field. The resolution improved to 200 psec after the modification of STC by changing the scintillator thickness from 3 mm to 5 mm.

mm in height, 70 mm in width and 5 mm in thickness. They covered from ±12 degrees to ±54 degrees horizontally, and were placed 2615mm from the center of the spectrometer magnet.

2.5.2 Aerogel Čerenkov Counters

For the kaon trigger, the Aerogel Čerenkov counters (AC) were located just in front of the FTOF counters. Each AC was divided into 16 segments which geometrically matched with the FTOF segmentation.

The AC used about 500 litters of aerogel in total, with an active volume of 706 mm in height, 2640 mm in width and 125 mm in thickness in each arm, as summarized in Table 2.6. The aerogel was produced at the auto-crave facility in Mori-Seiyu Co. Ltd, by introducing new technology to produce hydrophobic aerogel [19]. The attenuation length of the aerogel is 25±4 mm at 400 nm. This is long enough to adopt the light collection scheme for Čerenkov photons, as shown in Figure 2.15.

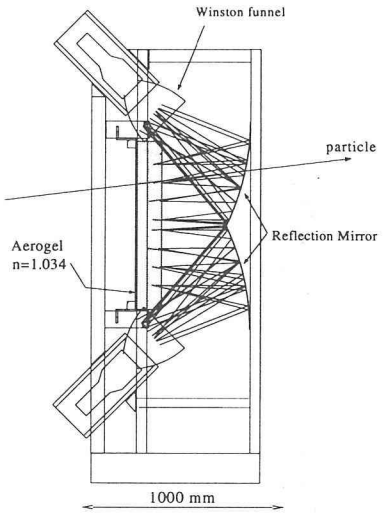

Figure 2.15: One segment of the Aerogel Čerenkov Counter and the light collection scheme.

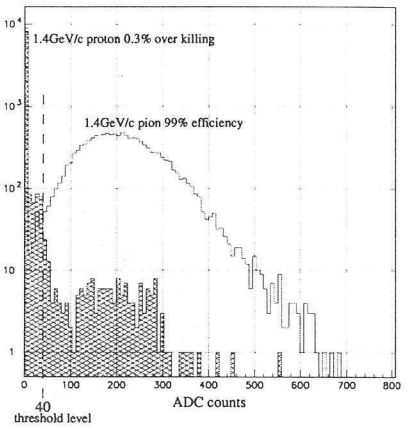

Figure 2.16: Pulse height distribution of AC for the 1.4 GeV/c π^+ and proton. When we set the threshold at 0.5 photoelectron level the efficiency for pion is 99.0%.

The index of aerogel we made is 1.034±0.004, corresponding to the momentum threshold of 0.53 GeV/c for pions. The efficiency of AC was measured to be 99% for pions at 1.4 GeV/c as demonstrated in Figure 2.16. The details of the aerogel production and the counter design can be found in the reference [20].

2.6 Electron Identification Counters

The counters to identify electrons are other key elements of this spectrometer. The present analysis uses only kaon-identification counters so that the simple descriptions are given here.

Electrons are identified as a coincidence signal of the two stages of the electron-identification counters. The front stage is two sets of the gas Čerenkov counters called FGC which cover from ± 6 degrees to ±90 degrees horizontally and segmented into 13 units in each arm. The vertical acceptance covers ±23 degrees. The rear stage is different according to the acceptance regions. In the kaon-arm acceptance, the rear stage is also the gas Čerenkov counters called RGC which has 7 segments in each arm matching with the FGC segmentation. The cross section of the electron-identification counters in the kaon acceptance is schematically shown in Figure 2.17, together with the light collection scheme in the gas Čerenkov counters.

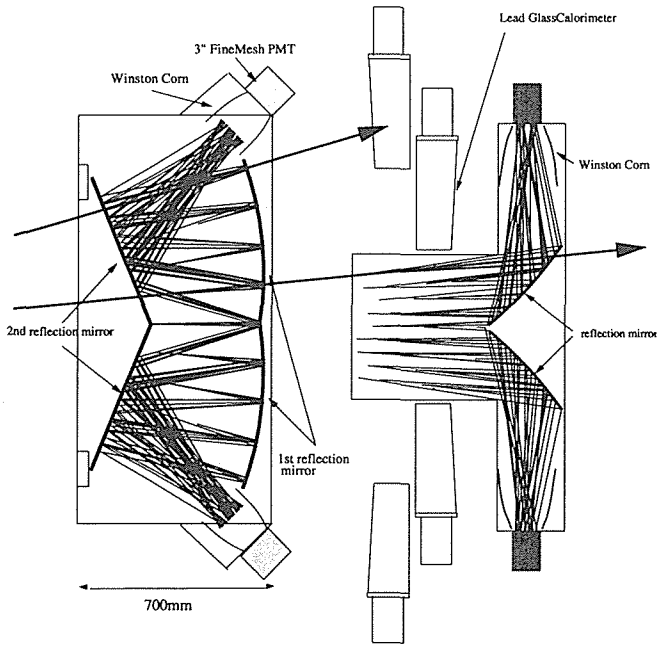

Figure 2.17: The cross section of FGC, RGC and REMC.

Both types of the Gas Čerenkov counters use isobutane (n=1.00127) as radiator. Aluminum evaporated mirrors and Winston funnels are used to collect Čerenkov photons. In FGC to operate under the magnetic field of 0.2T, 3-inch fine-mesh PMT's are used. Since the vertical acceptance is smaller in the kaon arm than in the electron arm, the rear lead-glass EM calorimeters (REMC) are placed to cover the rest of the acceptance as seen in Figure 2.17. The REMC's use the lead-glass (SF6W) counters recycled from the EM calorimeter of TOPAZ at TRISTAN.

In the horizontal angular regions larger than 57 degrees are covered with the lead-glass counters called SideEMC (SEMC), using also the TOPAZ EM calorimeters. The layout is shown in Figure 2.18. We disassembled the TOPAZ calorimeter modules and used only the lead-glass blocks. We reshaped and repolished the blocks in Tochigi Nikon Corporation into a rectangular shape from the original tapered shape. Five units of the lead-glass blocks were stacked vertically and glued by epoxy resin to form one segment unit of the calorimeter viewed by a pair of PMT's from the top and the bottom ends. Čerenkov photons from an EM shower are transported to the PMT's by total reflection along the surface of the lead glass. The SEMC's are a hodoscope-like structure with 9 segments in each arm. They are located behind BDC and fixed onto the return yoke of the spectrometer magnet.

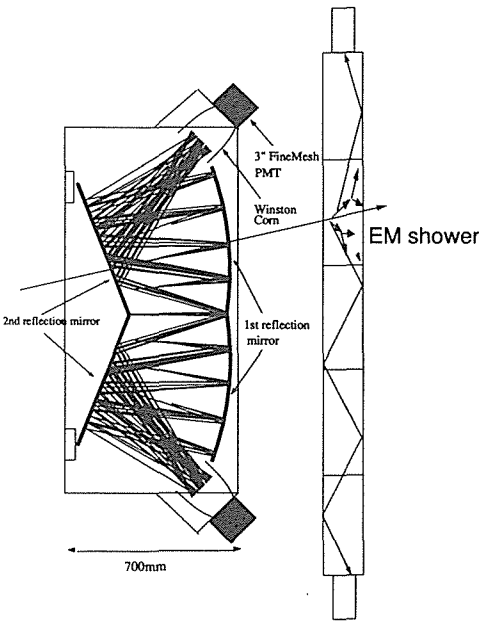

Figure 2.18: The cross section of FGC and SEMC.

The pion rejection efficiency and electron identification efficiency of these counters are summarized in Table 2.7. In the combination of the front and the rear stage, pions are rejected to about 10^{-3} which satisfies the requirement of the $\phi \to e^+e^-$ decay measurements.

	FGC	RGC	REMC	SEMC
pion rejection efficiency(%)	96.6	96.5	98.0	98.0
electron ID efficiency(%)	85	83	90	90

Table 2.7: Performance of the electron identification counters. For REMC and SEMC, the values are for the momentum range greater than 500MeV/c.

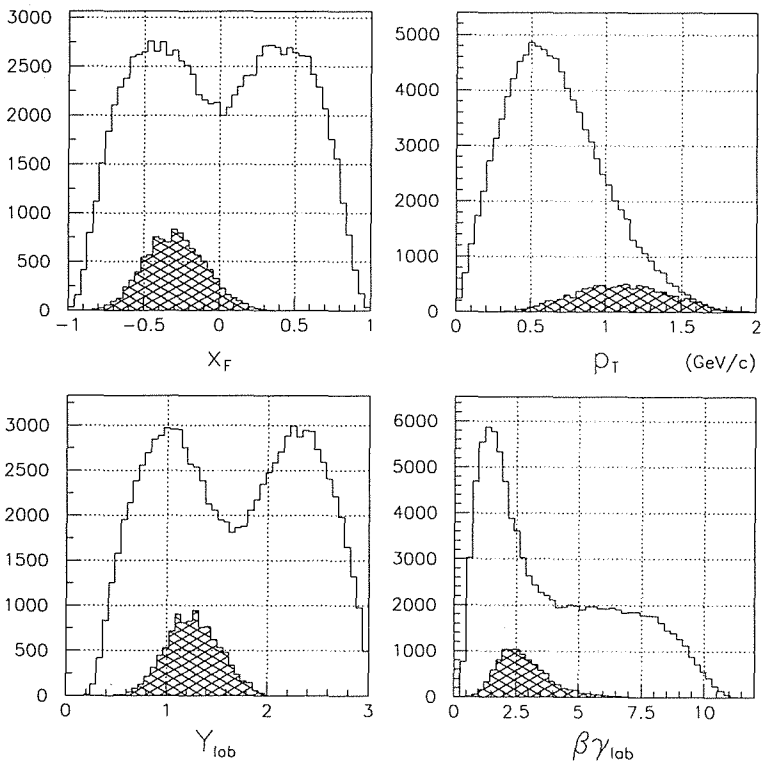

Figure 2.19: The assumed kinematical distributions of the ϕ meson production. The dependence of x_F , p_T , rapidity and $\beta\gamma_{lab}$ are shown. The spectrometer acceptance is shown as hatched areas after multiplied by factor 25. The vertical axes are in an arbitrary unit.

2.7 Spectrometer acceptance

The spectrometer acceptance was optimized to gain the acceptance for ϕ mesons with low $\beta\gamma_{lab}$ to maximize the decay probability inside nucleus. In the optimization we adopted the p_T and the x_F distributions measured in the 11.75-GeV/c $pp \rightarrow pp\phi$ reaction [21], since the kinematical distribution of the ϕ production is unknown in 12-GeV $p + A$ interaction.

Figure 2.19 shows the results of Monte Carlo calculations, the x_F , p_T , rapidity and $\beta\gamma_{lab}$ dependences of the assumed distribution, together with the same distributions of the detected events in the spectrometer in the $\phi \rightarrow K^+K^-$ decay mode. Typical acceptance is 1.0 % with a peak around $\beta\gamma_{lab} = 2$. For low energy ϕ mesons, the acceptance decreases due to the kaon decays.

2.8 Trigger

Three-level trigger logic was adopted to obtain the K^+K^-events in the experimental period described in this manuscript. The scheme of the trigger logic is shown in Figure 2.20.

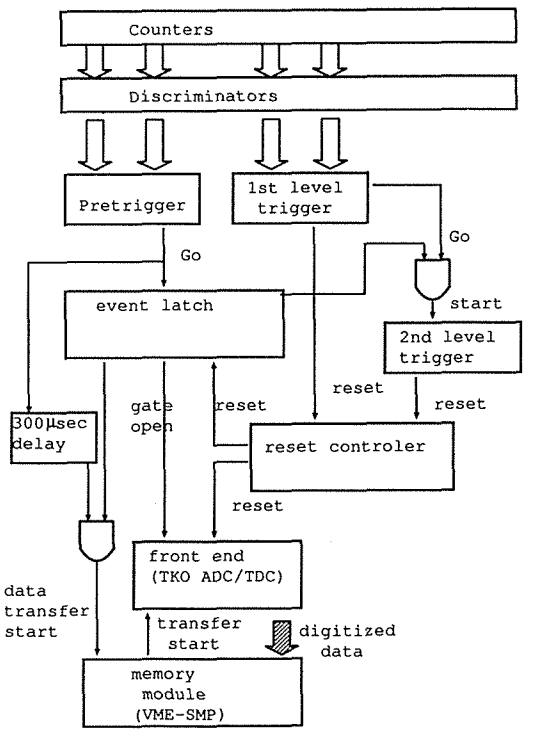

Figure 2.20: Trigger scheme.

The Pre-trigger (0th-level trigger) was used to open the gate of all the ADC and the TDC modules. At this level the logic was made of NIM modules defining two-track candidates by requiring at least one hit in STC and at least two hits both in FTOF and HC, where FTOF hits were required not to be accompanied with a AC hit in the same arm. The decision time in this level was 30 nsec.

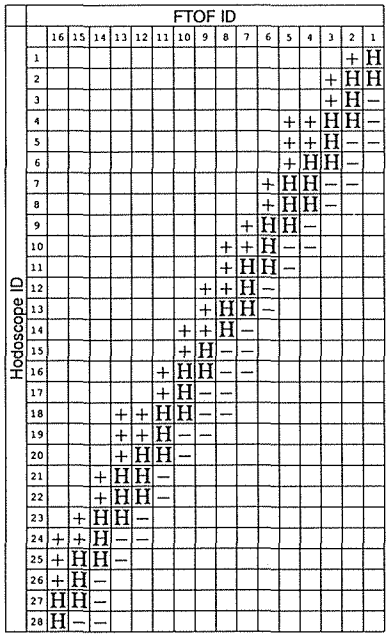

Figure 2.21: The pattern of the matrix coincidence in the 1st-level trigger logic. 'H' means 'high momentum', and '+' and '−' are for the positive and negative tracks, respectively.

Pions whose momentum are greater than 0.53 GeV/c generate a signal in AC. The AC signal was used to veto those pions. It should be noted that in the present data the logic worked as an AC hit vetoed all the FTOF counters in the same arm. This simplified veto logic caused overkilling of the events when other pions entered in the same arm as the kaon. The rate of the overkilling was evaluated in the off-line analysis using the data taken without the AC veto. We found that the survived event rate from the overkilling were 39.2±0.6%, 38.8±0.6%, 45.7±0.5% for the targets, polyethylene, carbon and lead, respectively[†]. This values were used to

[†]The fact, that the lead target has a smaller overkilling rate than carbon, looks contradictly to the multiplicity increases with the mass number. According to reference [23], measuring the the particle productions in 4-GeV $p + A$ interaction, the increase of multiplicity is due to the proton production and the pion multiplicity tends to decrease with the mass number due to the pion absorption by nucleus.

correct the target dependence of the production cross section of ϕ meson .

The 1st-level trigger was a matrix-coincidence logic of FTOF and HC to select oppositely-charged track-pairs. This logic was implemented with the hand-made modules using Field Programmable Gate Arrays (FPGA, Lattice ispLSi 3256). The decision time in this level was about 250 nsec. The charge of the track candidates was determined as the matrix pattern shown in Figure 2.21, where '+' and '−' are the determined signs and 'H' denotes a high momentum track with an undefined charge. At least one positive and one negative track were required, and the high momentum track (H) were considered to be either charge, i.e., $+-$, $+H$, $H-$ and HH combinations were allowed. This requirement covered the momentum range greater than 0.4 GeV/c. The 1st-level trigger logic worked in parallel with the 0th-level trigger logic. When these conditions were not satisfied, this logic generated a reset signal to the digitizer modules. Typical reduction on the trigger rate was 25%.

The 2nd-level trigger used the timing information from the FTOF counters and select particles with their velocity. A timing window was set commonly for all the FTOF counters to exclude the particles outside the TOF range set for kaons whose momentum was in the range from 0.5 to 1.2 GeV/c. This logic was started by the accepted 1st-level signal. When the condition was not satisfied, this logic generates the reset signal to the digitizer modules. The decision time in this level was less than 100 μsec. By this trigger, we obtained 55 % reduction in the trigger rate, and observed K^+K^-pair enhancement of factor 4 in the final data sample compared with the case when only the 1st-level trigger was applied.

This logic was also implemented with the hand-made modules [22] using FPGA's (Xilinx XC3190A) together with the fast timing measurements done by the Lecroy FERA/FELET modules. The 2nd level trigger was adopted partially during the data taking period.

When the reset signal from the 1st- and the 2nd-level trigger were not issued in 300μsec, the data transfer sequence from the digitizer modules to the memory module was started. Typical transfer time was 300μsec.

Typical trigger rates of each level are shown in Table 2.8. The 0th- and the 1st-level triggers were down-scaled and recorded through the data taking period. Typical "live time" of the data acquisition was 20%.

trigger	0th	1st	2nd
logic	NIM	FPGA(Lattice)	FPGA(XilinX)
decision time	30ns	250ns	100μsec
typical request rate(/spill)	12K	9K	4K

Table 2.8: Trigger rate summary.

2.9 Data Acquisition

Online Data Acquisition was controlled with Hewlett-Packard Model 743, on-board workstation (HP) in the VME crate. Operating System HP-RT 2.0 was running on this workstation. The schematic view of the data acquisition system is shown in Figure 2.22.

All the event data from the spectrometer were digitized with TKO modules [24], which are the KEK standard. The CAMAC modules were used to record the status of the experiment such as scaler counts of the detectors. Data from the TKO modules were transferred event by event to the VME-SMP memory modules

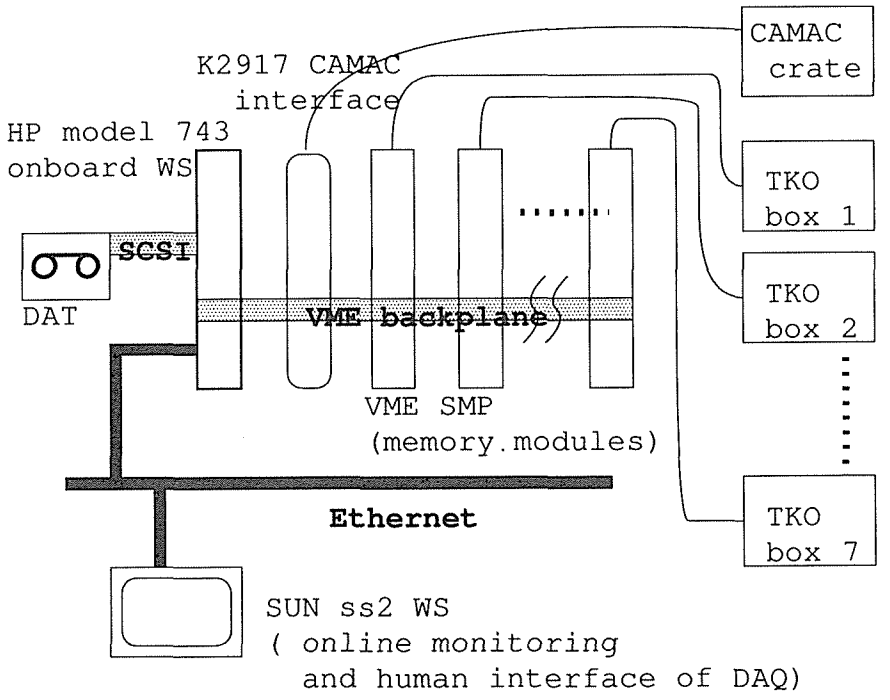

Figure 2.22: The schematics of the data acquisition system.

in the VME crate. Typical transfer time was 300 μ sec. The CAMAC modules were controlled via Kinetic K3922 Crate Controller and Kinetic K2917 CAMAC-VME interface in the VME crate.

During the beam-off period between two spills, the data on the VME-SMP modules and the CAMAC modules were transferred to HP via VME-bus, and then written to the Digital Audio Tape connected with HP via SCSI. The start timing of this transfer sequence was given by the spill-end signal from the accelerator. Typical transferred data size was about 1M byte per spill, corresponding to 1000 events per spill.

Data were monitored using the on-line analysis program written in the Sun SPARCstation–2 workstation. Sample Data were transferred from HP through Ethernet using the TCP/IP protocol.

Chapter 3

Analysis

The analysis has been performed for the data collected for 15 days in June 1997, and the results are reported in this manuscript. This period was the first physics run of this spectrometer system.

We collected about 1.0×10^8 events in the kaon pair trigger using 1.12×10^5 spills corresponding to 1.54×10^{13} protons on target. After the necessary calibrations and the alignment as described in the previous chapter, we performed a simple track reconstruction which based on the quadratic fitting on the hit positions in CDC, and the BDC hits were connected to the track. As the first step of the event reduction, we required at least one positive and one negative charged tracks to be reconstructed with the position matching with a FTOF hit. About 3×10^6 events survived this process.

Next, good tracks were selected with the timing information from the scintillation counters. Timing infomation given by the FTOF and the HC counters, which geometrically matched with the tracks found in CDC, was used to discard fake track candidates such as ones going out of the vertical acceptance of the kaon arms. Since no vertical position information were used in our trigger scheme, the vertical information is effective to reduce the background tracks. At this stage, we required the track pairs to have the TOF values consistent with kaon. Since the simple momentum determined only with the CDC hits is not precise, we required calculated mass

m to be in the range of $0.2 < m < 0.8$ GeV/c^2. About 4×10^4 events survived after this requirements, including 1.2×10^4 events in which the both charged tracks were in the same arm.

In the last step, the survived tracks were fitted with the Runge–Kutta method and their momenta were determined. They were used to obtain the invariant mass distribution of the K^+K^-pairs. Detail descriptions of the analysis procedure are given below.

3.1 Track reconstruction

The track reconstruction was performed in three steps. First, the track candidates were searched in CDC in the horizontal plane using only the X-X' layers. The candidate must have at least 5 hits from the 6 X-X' layers.

Usually a hit in the drift time recorder was regarded as two independent hits in the drift space to include the left-right ambiguity. When the X-X' combinations allowed to select either drift direction, those two hits were regarded as one hit-pair.

Then all the possible combinations of the hits or the hit-pairs were compared in terms of the χ^2 with the quadratic fit. The best-χ^2 candidate was selected as a *horizontal track* for each hit or hit-pair in the inner X-X' layers.

Second, the tilt layers in CDC were searched for each *horizontal track*. At least 3 tilted wires were required from the two U and two V layers. In principle, the track candidate having the best χ^2 was picked up as a *spatial track* among all the possible combinations of the U-V layers for each *horizontal track* selected above.

Since there was a tendency that the 3-hits combinations in the U-V layers had smaller χ^2 than the 4-hit combinations, we adopted a selection algorithm as follows. We compared the 3-hit combinations and the 4-hit combinations independently. When the best 3-hit combination was the subset of the best 4-hit combination we select the 4-hit combination as a *spatial track*, otherwise candidate having the smallest χ^2 was selected. For all the *spatial tracks* we adopted the χ^2 cut corresponding to the reduced χ^2 being better than 4.5.

Third, BDC hits were searched for the tracks found in CDC. We extrapolated the CDC *spatial track* to BDC, where the extrapolation was approximated empirically with the momentum and the vertical angle of the CDC track.

In BDCs, possible hit combinations consisted of at least 3 hits from the 4 layers (X,X',U,V) were made. For each CDC track extrapolation, the horizontal position and the horizontal incident angle at BDC were compared with those obtained with

the BDC hit combinations to select track candidates. The position and the angle matching are plotted in Figure 3.1 and 3.2 together with the cut positions. Those were obtained as follows.

To select the best BDC hit combination for each CDC track, we made a linear fit

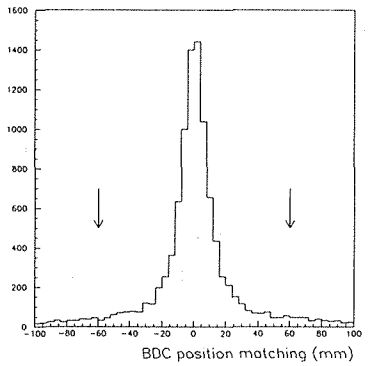

Figure 3.1: BDC position matching to CDC tracks. The arrows indicate the cut region.

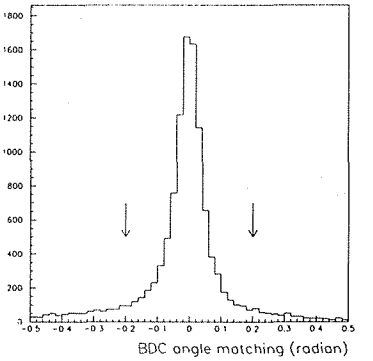

Figure 3.2: BDC angle matching to the CDC tracks. The arrows indicate the cut region.

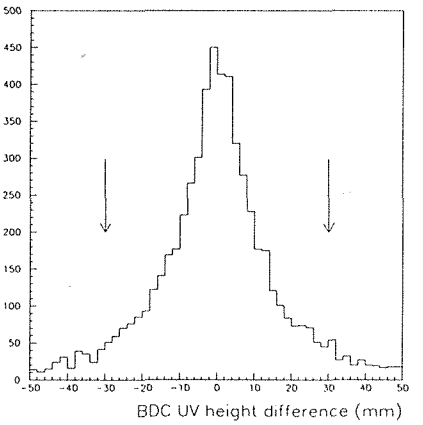

Figure 3.3: Height difference between the U and the V layers and the cut windows in BDC. The candidates in between the arrows are selected.

on the hit positions of all the 4 BDC layers projected to the xy-plane and obtained a χ^2 value. The hits in the U-V layers were projected using the track height information obtained from the extrapolated CDC track. If the BDC hit combination had both U and V hits (double-tilt combination), the height difference between the U hit and the V hit was also obtained as shown in Figure 3.3 using the horizontal position of the extrapolated CDC track. We selected candidates in the cut windows shown in Figure 3.1, 3.2 and 3.3. When more than two candidates existed, we picked up one with the best χ^2 value as follows.

Among the single-tilt combinations containing either U or V hit, the candidate having the best χ^2 in the xy-plane was selected from those satisfied the horizontal position and the angle matching. For the double-tilt combinations, the candidate having the least height difference was selected. When the best single-tilt combination was the subset of the best double-tilt combination, we selected the double-tilt combination as a real track, otherwise a candidate having the smallest χ^2 was selected. Sometimes a BDC hit combination was shared by two or more CDC tracks. Then we chose the CDC track giving the best matching parameter (the smallest height difference for the double-tilt combination or the smallests χ^2 for the single-tilt combinations). When there are two or more tracks have a common hit, we selected best χ^2 candidate in the CDC fitting and discarded others.

3.2 Counter matching with simple tracks

Before starting the time-consuming Runge–Kutta fitting, the simple counter matching with the track position was performed with an approximated trajectory of the track in order to reduce the number of events to be processed. The trajectory was approximated to a circle in the xy-plane in CDC and a line tangent to the circle was defined at the most outer layer in CDC. A cross point of the line at the counter position were corrected empirically from the data and the position matching is required to be within two units of the counter segmentation as shown in Figure 3.4. Additionally, we required both the FTOF and the HC hits had good vertical correlations each other (in Figure 3.5) and with the CDC track. When multiple combinations existed in the matching windows, one with the best correlation in the vertical directions were selected.

Counters selected in this simple method agree with those selected with the trajectories obtained by the Runge–Kutta method within 95%.

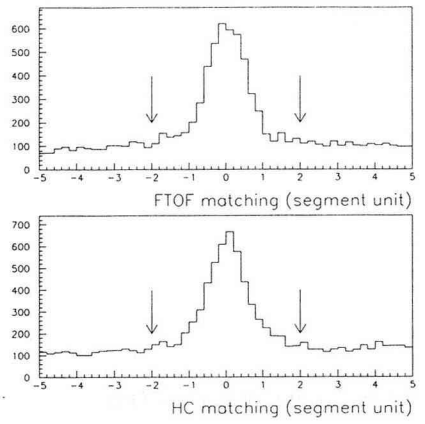

Figure 3.4: Horizontal position matchings of the FTOF and the HC with the CDC tracks, the upper figure for FTOF and the lower for HC.

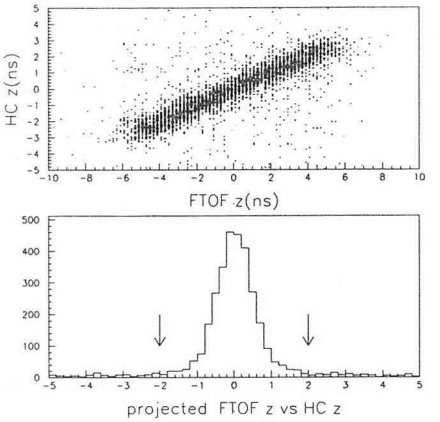

Figure 3.5: Vertical correlation between the FTOF hits and the HC hits connected to the same CDC track .

3.3 Track fitting

The track candidates were fitted finally with the Runge–Kutta method and their momenta were determined. Track tracing was performed in a 50-mm step using the magnetic field map calculated with TOSCA. The tracing started from the initial coordinates on the surface of a virtual cylinder of 100 mm in radius placed vertically at the center of the spectrometer magnet. The initial position and three components of the momentum vector were determined by the track found in CDC.

The search for the track parameters was performed using the minimization code MINUIT [25] to minimize the χ^2. The reduced χ^2 distribution is plotted in Figure 3.6. Using these tracks, invariant mass spectra of the K^+K^-pairs were reconstructed as described in the following chapter.

We have evaluated the multiplicity dependence of the track reconstruction efficiency since it is important to obtain the mass number dependence of the production cross section. First we examined the FTOF hit-multiplicity dependence of the track-reconstruction efficiency, and found that the difference of the efficiency was less than 10% between the multiplicity of 2 and 3 in one arm. When we observed a K^+K^-pair in one arm, the difference of the average values of the FTOF hit-multiplicity of the arm was only 2% between the carbon and the lead target data. Thus this effect is negligible in the present analysis.

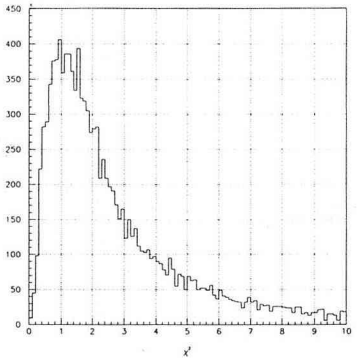

Figure 3.6: The reduced χ^2 distribution in Runge–Kutta fitting.

3.4 Particle identification and target determination

After the Runge–Kutta fitting, the tracks were again required to have the position matching with HC and FTOF. The matching was required to be within 2 units of

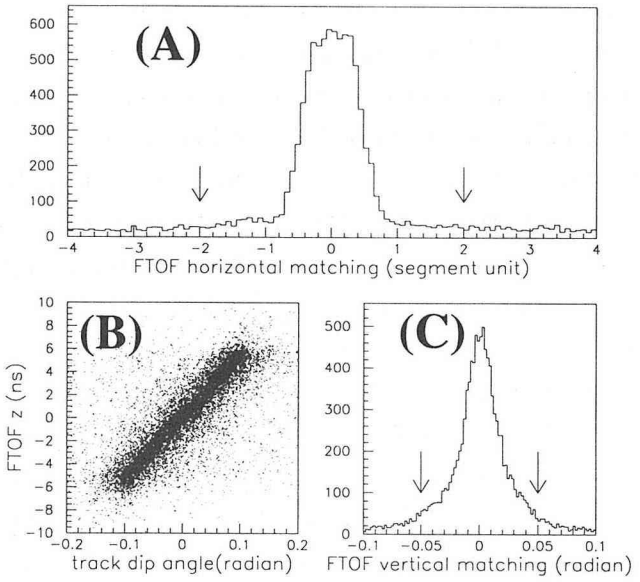

Figure 3.7: The position matching of the track fitted with Runge–Kutta method with the FTOF counters. (A) shows the horizontal matching and arrows indicate the cut region. Correlation in the z direction between the track and FTOF hit is shown in (B), projection of (B) is shown in (C) and the cut region is shown by the arrows.

the counter segment horizontally for HC and FTOF as shown in Figure 3.7 (A), and within about 0.05 radian vertically for FTOF as shown in Figure 3.7 (C), where z position of FTOF was obtained by the timing difference between the top PMT and the bottom PMT.

The length L from STC to FTOF along the trajectory was also obtained in the Runge–Kutta fitting. From the determined momentum p and measured time-of-flight T, the mass m of the particle was obtained as:

$$m = \frac{p \times \sqrt{(1-\beta^2)}}{\beta}, \qquad \beta = \frac{L(mm)}{T(ns) \times 299.792458}$$

The distribution of the reconstructed masses for positively charged tracks is shown in Figure 3.8. The hatched area is for the particles whose momenta are less than 0.8 GeV/c. The particles in the regions indicated in Figure 3.8 were considered to be kaons, corresponding to $0.4 \leq m \leq 0.6$ GeV/c^2. This window is used to determine the width and the resonance peak position of the ϕ meson.

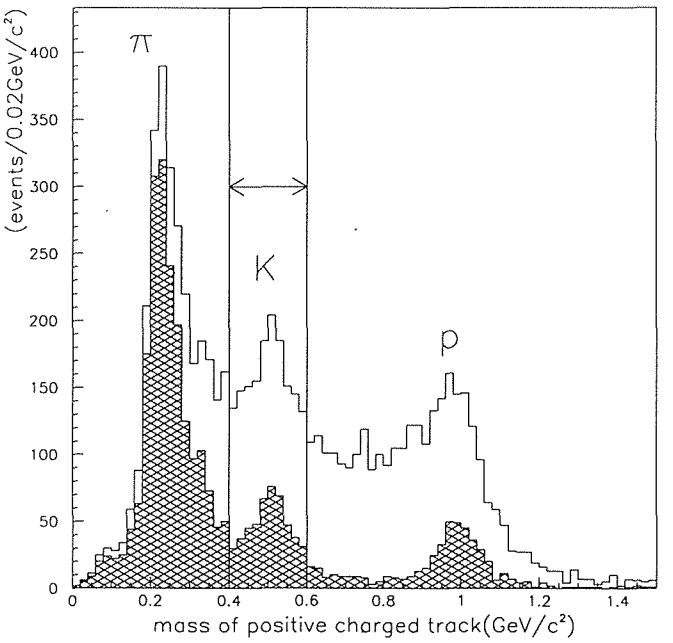

Figure 3.8: The distributions of the reconstructed mass obtained from the Runge–Kutta fitting and the time-of-flight measurements. The hatched area is for the particles whose momenta are less than 0.8 GeV/c. The most of pions and protons are eliminated in the event selection before the Runge–Kutta fitting, so that only small fractions of those particles are seen in this plot and the peak shapes are distorted.

The target vertex point was determined as the shortest distance point between two tracks. The vertex distributions are shown in Figure 3.9 for the events in which the tracks were detected in the different arms. The three targets are clearly seen. When the two tracks were in the same arm, the accuracy of the vertex-point

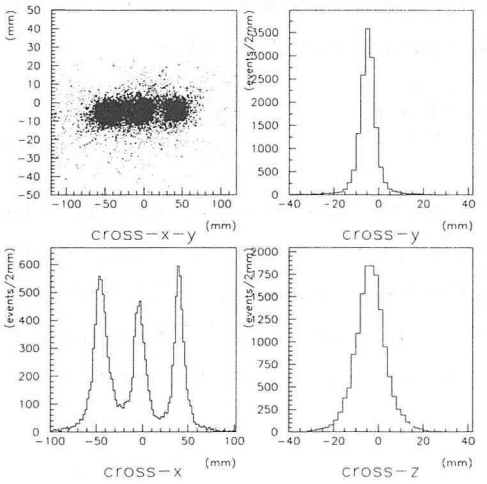

Figure 3.9: Reconstructed vertex distributions when the tracks were detected in the different arm.

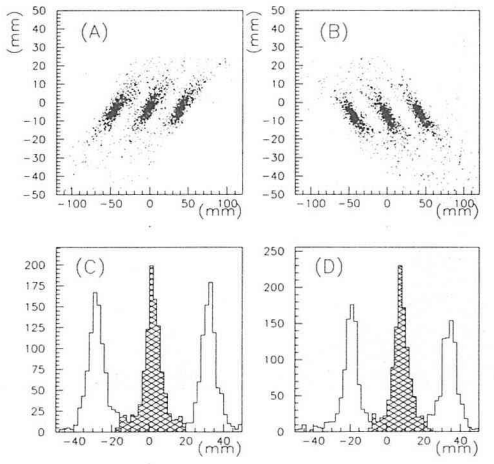

Figure 3.10: The target image in the x-y plane, (A) for the left and (B) for the right arms, when the two particles are detected in the same arm. The histograms are the projected distributions onto the directions of the corresponding arm. Hatched regions show the events determined as from the target at the center.

determinations got worse due to the narrow opening angle between the two tracks. In this case we used the target-image distribution viewed from the direction of the kaon arm as shown in Figure 3.10. The three targets are still clearly distinguished. Last, we required the y-coordinate of the vertex to be within 30 mm from the peak position.

Chapter 4

Results and Discussion

4.1 Resonance position and width of observed ϕ mesons

The invariant mass spectra of K^+K^-pairs detected in the same arm are shown in Figure 4.1 for three different targets, polyethylene, carbon and lead. Clear resonance peaks corresponding to $\phi \rightarrow K^+K^-$decays are observed. To examine the resonance positions and the widths, we have applied rather strong conditions to select the events as follows.

For the particle identification, the reconstructed mass m was required to be in the range $0.4 \leq m \leq 0.6$ GeV/c^2 to select kaon severely, and reduced χ^2 of the Runge–Kutta fit is required to be less than 3 to eliminate possible mis-trackings (*strict cut*). Additional cut was applied to reduce the background using the correlation of the trajectories of K^+ and K^-. Since the decay Q-value is as small as 32 MeV/c^2 , the opening angle at BDC measured from K^- to K^+ is always in the same sign. This relation was required for the K^+ and K^- tracks in the data. To evaluate the shape of the background, the event-mixing method was applied. We have assumed that the background is due to an uncorrelated pair of particles so that the two tracks from different events should have the same distribution as the background shape. The hatched areas in the Figure 4.1 are the shape obtained by the event mixing. We did not use K^+ and K^- in the ϕ peak ($1.01 < M_{K^+K^-} < 1.03$ GeV/c^2) in the event mixing to eliminate a possible correlation due to the $\phi \rightarrow K^+K^-$kinematics.

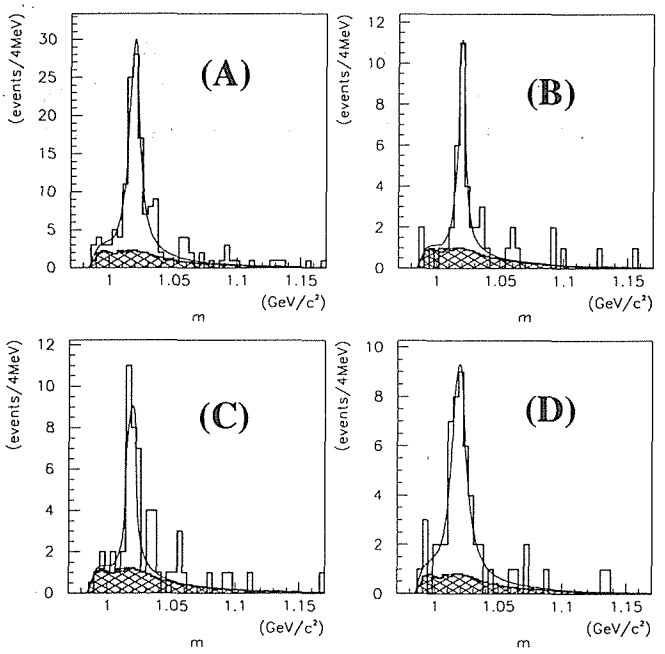

Figure 4.1: The invariant K^+K^- spectra obtained with the strict cut. In (A) we include all the three target. The spectra (B),(C) and (D) are corresponding to polyethylene, carbon and lead targets respectively. The hatched areas are the backgrounds evaluated by the event-mixing method.

target	resonance (MeV/c^2)	observed width (MeV/c^2)	compensated width (MeV/c^2)
Polyethylene	1019.6 ± 0.9	5.9 ± 2.4	5.3 ± 2.4
Carbon	1018.1 ± 0.9	5.4 ± 2.8	4.9 ± 2.8
Lead	1018.5 ± 1.6	11.9 ± 5.0	11.5 ± 5.0
natural width [18]	1019.413 ± 0.008	4.43 ± 0.05	-

Table 4.1: The resonance position and the width of the observed ϕ mesons.

The spectra were fit with the sum of the Breit–Wigner function and the background shape $B(M_{K^+K^-})$,

$$\frac{dN}{dM_{K^+K^-}} = \alpha \times \frac{(\Gamma/2)^2}{(M_{K^+K^-} - M_0)^2 + (\Gamma/2)^2} + \beta \times B(M_{K^+K^-})$$

where α and β are the amplitude to be determined, and Γ and M_0 are the width and the position of the resonance to be examined.

The best fit values of the parameters are listed in Table 4.1. We have subtracted the effect of the mass resolution evaluated from the width of Λ (mentioned in Section 2.4) from the observed widths. The resonance positions and the widths are plotted in Figure 4.2. The resonance positions obtained by the present work are consistent

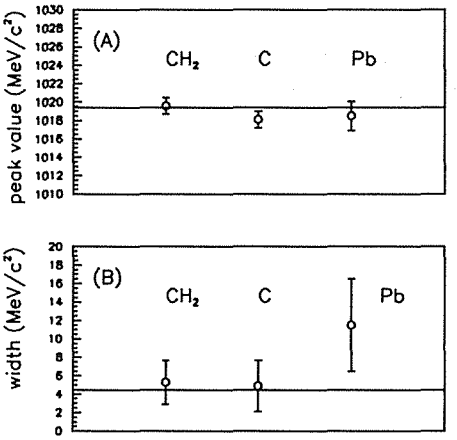

Figure 4.2: The resonance position (A) and the width (B) of the observed ϕ mesons. The line is drawn at the values in free space.

with the known value of 1019.4 MeV/c^2 in the reference [18]. The widths of ϕ meson from the polyethylene and the carbon target are also consistent with the natural width of ϕ meson, 4.43±0.05 MeV/c^2, within one sigma. For the lead target case, the width looks larger but the statistical significance is not enough to conclude the difference.

The p_T , rapidity, and $\beta\gamma_{lab}$ distributions of the observed ϕ mesons in the range of 1.01 $< M_{K^+K^-} <$ 1.03 GeV/c^2 are shown in Figure 4.3. The momentum distribution of K^+ and K^- are also shown in Figure 4.4 with the same event selection. We summed up the events from all the target. We have not observed any significant difference in the distributions among the three targets.

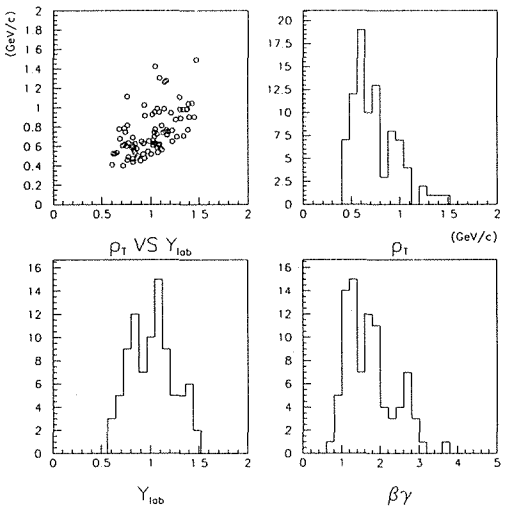

Figure 4.3: p_T, *rapidity* and $\beta\gamma_{lab}$ distributions of the observed ϕ mesons. The central rapidity Y^{pp}_{CM} is 1.62.

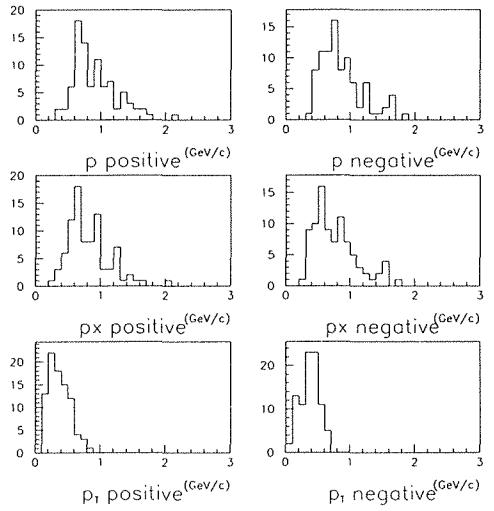

Figure 4.4: The momentum distributions of the kaon pairs of the observed ϕ mesons.

4.2 Mass number dependence of production cross section

To obtain the yield of ϕ mesons, we loosen the particle identification cut and the χ^2 cut on the tracks to obtain more statistics (*loose cut*). This treatment increases the background as well as the yield of ϕ mesons. After the same procedure as the previous section the invariant mass spectra are obtained as shown in Figure 4.5.

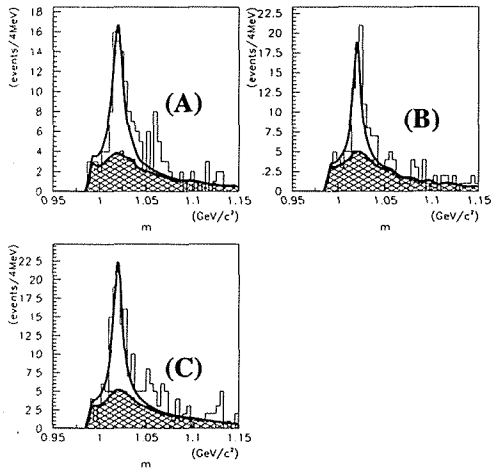

Figure 4.5: The invariant K^+K^- spectra with loose cut. (A), (B) and (C) are corresponding to polyethylene, carbon, lead targets respectively. The hatched areas indicate the backgrounds evaluated by the event-mixing method.

	polyethylene	(hydrogen)	carbon	lead
all p_T with loose cut	59.2 ± 13.4	(7.5 ± 8.3)	57.0 ± 12.8	74.1 ± 14.1
p_T ≤0.7GeV/c	40.6 ± 15.2	(11.2 ± 8.3)	23.6 ± 8.5	34.3 ± 11.2
p_T >0.7GeV/c	26.4 ± 9.3	(1.1 ± 6.0)	31.3 ± 9.7	40.4 ± 9.8
all p_T with strict cut	23.5 ± 7.9	(−0.1 ± 5.0)	30.5 ± 8.0	36.2 ± 10.8

Table 4.2: Number of observed ϕ mesons.

The yields of the ϕ mesons are listed in Table 4.2, which were obtained by

subtracting the background function bin by bin in the mass region of 1020 ± 22 MeV/c^2. The background yield was determined by the fit. The hydrogen data were obtained by subtracting the carbon data from the polyethylene data.

We analyzed the mass number dependence of the production of ϕ meson using the standard parametrization,

$$\sigma(A) = \sigma(A = 1) \times A^{\alpha}, \tag{4.1}$$

where A is the atomic mass number of the target nucleus. The production cross section of ϕ meson can be written as:

$$\sigma_{\phi} = \frac{N_{\phi}/\varepsilon}{N_{beam}\rho l}$$

where N_{ϕ} is the number of the observed ϕ mesons, ε is the detection efficiency, N_{beam} is the number of beam particles, ρ is the number density of the target and l is the target thickness.

Since N_{beam} was common for all the targets, we can extract the α parameter from two targets as follows:

$$(\frac{A_{Pb}}{A_C})^{\alpha} = \frac{\sigma_{\phi}(Pb)}{\sigma_{\phi}(C)} = \frac{N_{\phi Pb}}{N_{\phi C}}\frac{\varepsilon_C}{\varepsilon_{Pb}} * \frac{\rho_C l_C}{\rho_{Pb} l_{Pb}}$$

where subscripts Pb and C indicate the target materials. We adopted the difference in the detection efficiency ε due to the overkilling in the trigger using the aerogel-Čerenkov veto logic, as described in Section 2.8. The ratio $\varepsilon_C/\varepsilon_{Pb}$ was 0.849 ±0.016 and $\varepsilon_{CH_2}/\varepsilon_C$ was 1.010±0.022.

For the polyethylene-carbon subtraction, we adopted the same normalization except that we dealt the overkilling ratio to be unity. The cross section ratio for hydrogen is obtained as follows,

$$\sigma_{\phi}(H) = \frac{\sigma_{\phi}(CH_2) - \sigma_{\phi}(C)}{2}$$

The results are summarized in Table 4.3 and plotted in Figure 4.6 together with the best fit line of the parameterization of Equation 4.1. The fitting over three data points, hydrogen, carbon and lead gives a larger error than the results given by the ratio of $\sigma_{\phi}(Pb)$ to $\sigma_{\phi}(C)$.

The data from the strict-cut analysis described in the previous section were analyzed in the same way and gave a consistent result with the loose cut. The loose-cut data are divided into two p_T bins, fitted in the same way. The obtained α parameters by the ratio are listed in Table 4.4.

	polyethylene	(hydrogen)	carbon	lead
all p_T with loose cut	1.34 ± 0.31	(0.17 ± 0.19)	1 ± 0.22	16.5 ± 3.1
$p_T \leq 0.7$GeV/c	2.22 ± 0.82	(0.61 ± 0.45)	1 ± 0.36	18.4 ± 6.0
$p_T > 0.7$GeV/c	1.09 ± 0.38	(0.05 ± 0.25)	1 ± 0.31	16.4 ± 4.0
all p_T with strict cut	1.00 ± 0.34	(0.00 ± 0.21)	1 ± 0.26	17.7 ± 5.3

Table 4.3: Production cross sections of ϕ meson for each target normalized to that for carbon.

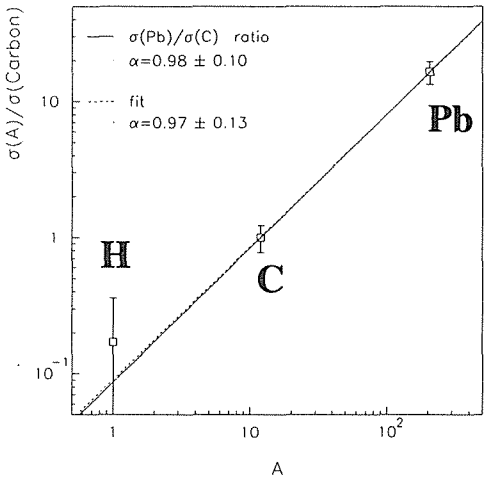

Figure 4.6: Mass number dependence of the cross section. The solid line is obtained by the ratio of $\sigma_\phi(Pb)$ to $\sigma_\phi(C)$. The dashed line is the best fit over the three points.

all p_T with loose cut	0.98 ± 0.10	
$p_T \leq 0.7$GeV/c	1.02 ± 0.17	mean $p_T = 0.56$ GeV/c
$p_T > 0.7$GeV/c	0.98 ± 0.14	mean $p_T = 0.98$ GeV/c
all p_T with strict cut	0.95 ± 0.14	

Table 4.4: The α parameters given by the ratio of $\sigma_\phi(Pb)$ to $\sigma_\phi(C)$.

4.3 Discussion

The present experiment is the first attempt to measure the production and the decay of ϕ mesons in the kinematical region where the effect of nuclear media should play an important role. The experiment was carried out with protons of 12-GeV incident energy, which is the lowest $\sqrt{s}$ amongst the ϕ-meson measurements in the hadron induced nuclear reactions. The obtained α parameter is plotted in Figure 4.7 together with other available data [13, 14] as a function of x_F of observed ϕ mesons. In spite of the large difference in incident energies and in kinematical coverage, the obtained α is consistent with those of other experiments.

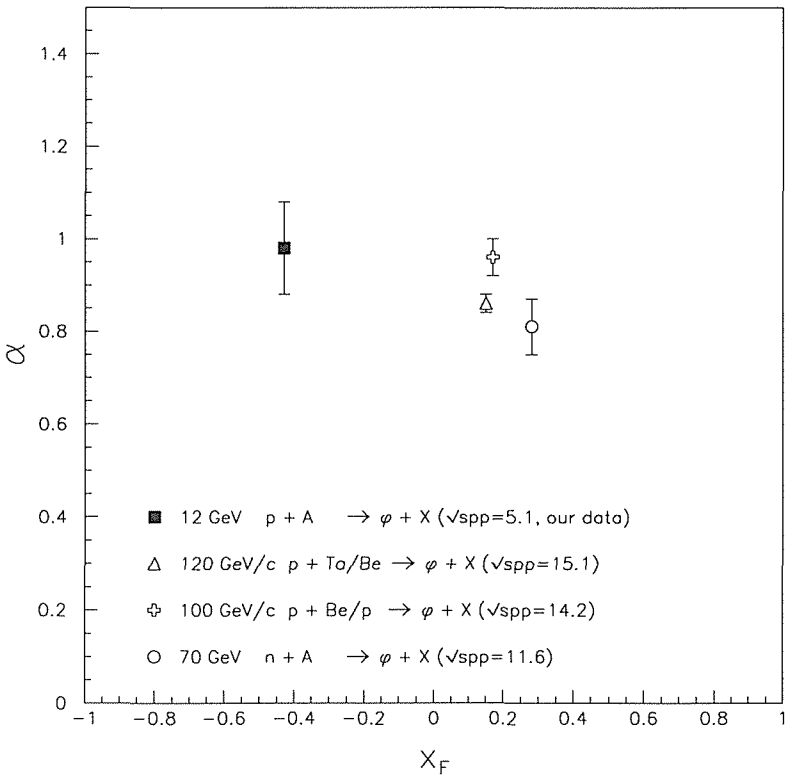

Figure 4.7: The x_F dependence of the α parameter.

Table 4.5 summarized the α parameters. The region of the transverse momentum p_T is higher in the present experiment than in others. One has to consider that the

Cronin effect [26], characterized by the increase of α as a function of p_T, can be the origin of the large α value obtained in the present experiment.

	$\sqrt{s}$ (GeV)	α	p_T (GeV/c)	x_F
12GeV $p + Pb/C$(present work)	5.1	0.98±0.10	0.4< p_T <1.5	$-0.8 < x_F < 0.3$ mean x_F=−0.43
120GeV/c $p + Ta/Be$[13]	15.1	0.86±0.02	0< p_T <1	0< x_F <0.3
100GeV/c $p + Be/p$[13]	14.2	0.96±0.04	0< p_T <1	0.11< x_F <0.24
70GeV $n + A$ [14]	11.6	0.81±0.06	0< p_T <1	0< x_F

Table 4.5: Comparison of the α parameters and the kinematic regions.

In the upper part of the Figure 4.8 we plot, the p_T dependence of α parameter of the present measurement, together with the α measurements in the 4.3-GeV/c $p + A \rightarrow \pi + X$ interactions [27].

In the pion measurements, the increase of α above $p_T = 0.6$ is attributed to the Cronin effect. We did not observe any increase of α in the ϕ meson production in the present data, although the statistical significance is limited. The origin of the Cronin effect is not well understood so far. One of possible explanations is the change of the production mechanism from non-perturbative interaction to perturbative one. If we assume the α value is determined with the Q^2 involved in the interaction, the plot of p_T dependence of α mentioned above should be re-plotted as a function of transverse mass, m_T, as is shown in the lower part of the Figure 4.8. The α value of the present data, then, is reasonably understood together with the α increase seen in the pion data.

The fact that the α parameter is close to unity at this energy region ($\sqrt{s} = 5.1$ GeV) is surprising. It is generally believed that incident energy of 12-GeV is dissipated rapidly and the nucleons in the back half of the nucleus can not contributed to the particle production. The present results suggests that the production mechanism of ϕ mesons is similar to that of J/ψ at higher energy, because the $s\bar{s}$ is heavy enough so that production from the fragmentation is greatly suppressed.

The observed widths of the ϕ meson for carbon and lead nuclei are consistent with the ones in free space. From the statistics presently available this does not mean that the media effect is absent.

According to the theoretical calculation of Klingl *et al.* [11], the in-medium decay width of ϕ meson increases as large as 45 MeV/c^2 at normal nuclear density,

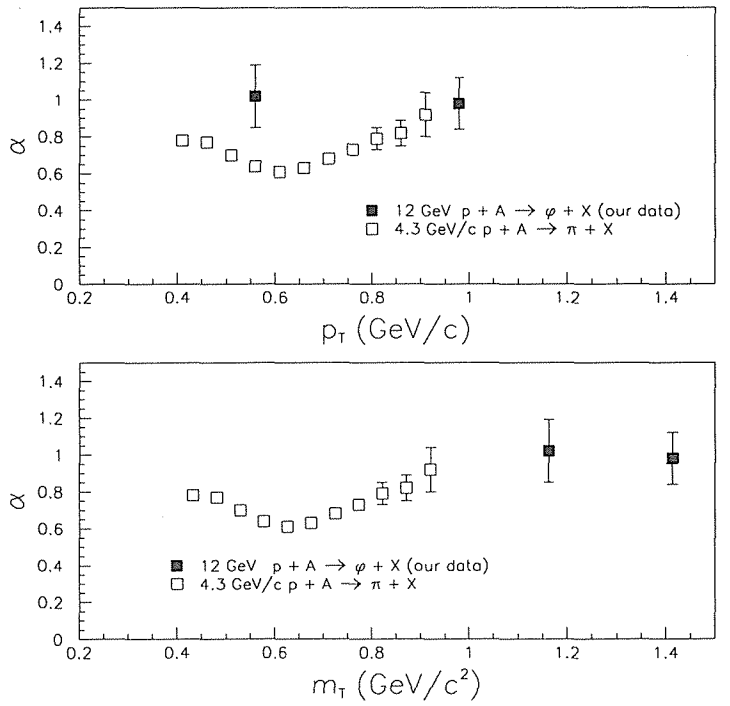

Figure 4.8: The p_T and m_T dependence of the α parameter.

i.e. its life time is reduced to 4.4 fm/c. As was explained in the Chapter 1 the calculation was made for the ϕ at rest, and the decay width is subject to change as the momentum of the ϕ meson increases. Thus their value should be considered as the maximum broadening of the ϕ meson in nuclear media, because the major mechanisms of the broadening is attributed to the K^-N interactions in nucleus and the interactions gets weaker as the K^- momentum increases.

The result that the α is close to unity suggests that the ϕ mesons are generated at anywhere in the lead nuclei. And the average $\beta\gamma_{lab}$ of the observed ϕ mesons from the lead target is 1.8. Taking into account these two facts, if the ϕ meson has 45 MeV/c^2 width in nuclei, about 40% of them are to decay and the broadened width of 45 MeV/c^2 could be seen. The effect of increase of decays inside nucleus should also be visible in the α parameter. Within the present statistics we could not conclude on the existence of such a broadened component especially because the amplitude of broadening is not known yet. Further data accumulation of the present experiment is desired both in the K^+K^-decay mode and the e^+e^-decay mode, to draw a conclusion on this interesting subject, nuclear matter modifications on the ϕ meson.

Chapter 5

Conclusion

We have observed the production and the decay of ϕ mesons in 12-GeV $p + A$ interaction, as the first results of the experiment E325 at KEK Proton Synchrotron. The experiment intends to measure the ϕ mesons for the first time in the kinematical region where the effects of the nuclear media should play an important role. The spectrometer was newly built for this purpose, characterized by the detection of slowly moving ϕ mesons both in $\phi \to K^+K^-$ and $\phi \to e^+e^-$ decay channels.

The K^+K^-invariant mass spectra for three different targets, carbon, polyethylene and lead, have been obtained. The widths of the resonance are 4.9±2.8 MeV/c^2 for carbon and 11.5±5.0 for lead, for the ϕ mesons with $\beta\gamma_{lab}$ in the region from 1 to 3. The widths as well as the resonance positions are consistent with those in free space, and any significant resonance-shape modification, which is expected from the in-medium modification of hadrons, was not seen within the statistical accuracy in the present study.

The mass number dependence of the production cross sections in the $\phi \to K^+K^-$ channel has been also obtained using carbon and lead targets. The parameter α is found to be 0.98 ± 0.10, very close to unity. This value is consistent with the ones measured at higher incident energies from 70 to 120 GeV using hadron induced nuclear reaction. The present work is the first measurement which covered the region of $x_F < 0$ closer to the target rapidity, while other measurements covered only $x_F > 0$. No significant p_T dependence has been observed on the α parameter, which suggests the steepness of the A-dependence of the ϕ production is not likely from the Cronin effect. It is noteworthy that such a large mass-number dependence is observed in the ϕ meson production at $\sqrt{s}$ as low as 5.1 GeV.

Acknowledgments

First of All, I would like to express my sincere gratitude to my supervisor, Prof. Hideto En'yo. He is a spokesperson of the experiment KEK–PS E325, and gave me the opportunity to join this experiment from the designing stage. Without his sincere and continuous support, insightful advice and tireless discussion, this work

would never been completed.

I also would like to express my special gratitude to Prof. A. Masaike and Prof. K. Imai. They introduced me to the field of particle and nuclear physics, and they have supported and guided me since my time in the undergraduate course.

I sincerely thank all the members of the KEK–PS E325 collaboration. I would thank Prof. J. Chiba for his advice and cooperation in the planning of this experiment and in the data analysis. I thank Profs. M. Ieiri and K. H. Tanaka for their work dedicated to the construction and the operation of the EP1–B beam line. Their expertise was also valuable in the construction of the spectrometer magnet. I also thank Mrs. M. Sekimoto for her work and advice in the chamber construction and the operation. I am very grateful to Dr. S. Mihara. He has built many of our detectors and organized the group in the preparation stage of this experiment.

Special thanks should be expressed to all the younger members in the collaboration. We took the beam–time shift together and have been analyzing the data together since then. M. Ishino's tireless work is very much appreciated. He has built the aerogel Čerenkov counters, and has been charged for the operation of all the counters. He also managed the PC–cluster for the analysis. All the tracking chambers were designed, fabricated and operated by K. Ozawa. I owe him a lot in the development of the track reconstruction program. I thank T. Tabaru who has been a key person of all the trigger and the electronics of this experiment. I also thank Y. Yoshimura for his work which realized the kaon 2nd–level Trigger. I am thankful to M. Naruki and T. Miyashita especially for their analysis of the TOF counters. I owe R. Muto and S. Yamada for the analysis of the magnetic field. They have measured the magnetic field map of the spectrometer and evaluated it with the calculations. I also thank T. Haseyama for his work in the magnet design.

I would like to express my thanks to Prof. H. Sakamoto and M. Suehiro for their help and advice for making the trigger modules using FPGA. I also thank Prof. T. Sumiyoshi and the members of the BELLE PID group, and Prof. H. Kawai and the members of the AIDA group for their guidance and advice about making the aerogel. The helpful guidance and advice to disassemble the TOPAZ EM calorimeter given by Prof. T. Tauchi and Dr. H. Yamaoka are appreciated very much. I am grateful to M. Hanabata, A. Ichikawa and Y. Kondo for their help in the fatiguing works like a cabling in the preparation period of this experiment.

I thank H. Kanda for his advice for the usage of the computer cluster system in KEK. I want to express my thanks to M. Yoshida and Dr. R. Susukita for their valuable guidance and discussions about the programming on the UNIX operating

system and the design of our data acquisition and monitoring system based on the Object–Oriented Programming using C++ programming language. I wish to thank Dr. H. Funahashi, Dr. M. Iinuma and Dr. Y. Matsuda for their guidance and grateful encouragement throughout my time in the graduate school. I also thank Dr. S. Yamashita for his advice about the simulation in the planning stage of this experiment.

The experiment was fully supported by the staffs of KEK, including the PS beam channel group, the PS floor staffs, the online group, the electronics division, and the accelerator division.

I would like to mention that in the analysis of this work and the preparations of this manuscript we used many free softwares including GNU C Compiler, LaTeX, Linux and so on. I appreciate the people engaged in such world–wide enterprises and especially thank those in Free Software Foundation.

This work was partly supported by Japan Society for the Promotion of Science and a Grant-in-Aid for Scientific Research of the Japan Ministry of Education, Science and Culture (Monbusho).

Bibliography

[1] T. Hatsuda and S. H. Lee, Phys. Rev. C46 (1992) R24

[2] T. Hatsuda and T. Kunihiro, Phys. Rep. 247 (1994) 221
G.E. Brown and M. Rho, Phys. Rep. 269 (1996) 333
W.S. Chung, C.M. Ko, G.Q.Li, Nucl. Phys. A641 (1998) 357
and references therein.

[3] G. Agakichiev *et al.*, Phys. Lett. B422 (1998) 405

[4] E.G. Drukarev and E.M. Levin, Prog. Part. Nucl. Phys. 27 (1991) 77

[5] K. I. Maruyama, Nucl. Phys. A629 (1998) 351c
G. J. Lolos *et al.*, Phys. Rev. Lett 80 (1998) 241

[6] http://www.e12.physik.tu-muenchen.de/hades/

[7] T. Kinashi *et al.*, In Hyogo 1997, Exciting physics with new accelerator facilities 55-62

[8] H. En'yo, KEK–PS E325 proposal (1994)

[9] R. Hayano *et al.*, GSI S214 proposal (1997)

[10] T. Yamazaki *et al.*, Phys. Lett. B418 (1998) 246

[11] F. Klingl, T. Wass, W. Weise, Phys. Lett. B 431 (1998) 254

[12] M.Binkley *et al.*, Phys. Rev. Lett. 37 (1976) 571

[13] C. Daum *et al.*, Z. Phys. C 18 (1983) 1
R. Bailey *et al.*, Z. Phys. C 22 (1984) 125

[14] A. N. Aleev *et al.*, JINR, D1-90-168(1990), Dubna

[15] Y. Sugaya *et al.*, Nucl. Instr. and Meth. A 368 (1996) 635

[16] Vector Fields Limited (UK). http://www.vectorfields.co.uk/

[17] developed in CERN. http://consult.cern.ch/writeup/garfield/

[18] Particle Data Group, Europ. Phys. J. C3 (1998) 376

[19] I. Adachi *et al.*, Nucl. Instr. and Meth. A 335 (1995) 390

[20] M. Ishino *et al.*, Nucl. Instr. and Meth. in preparation.

[21] M. W. Arenton *et al.*, Phys. Rev. D 25 (1982) 2241

[22] Y. Yoshimura *et al.*, Nucl. Instr. and Meth. in preparation.

[23] H. En'yo *et al.*, Phys. Lett. B159 (1985) 1

[24] T. K. Ohsuka *et al.*, KEK report 85-10(1985)

[25] developed in CERN. http://consult.cern.ch/writeup/minuit/

[26] J. W. Cronin *et al.*, Phys. Rev. D 11 (1975) 3105

[27] M.Ono *et al.*, Phys. Lett. B 84 (1979) 515